LEVEL II

12

AFWAL-TR-81-2018

AD A103023

VELOCITY MEASUREMENTS IN CONFINED DUAL COAXIAL JETS BEHIND AN AXISYMMETRIC BLUFF BODY: ISOTHERMAL AND COMBUSTING FLOWS

UNIVERSITY OF DAYTON
RESEARCH INSTITUTE
DAYTON, OHIO 45469

APRIL 1981

INTERIM REPORT FOR PERIOD OF JANUARY 1979 to SEPTEMBER 1980

Approved for public release; distribution unlimited

DTIC FILE COPY

AERO PROPULSION LABORATORY
AIR FORCE WRIGHT AERONAUTICAL LABORATORIES
AIR FORCE SYSTEMS COMMAND
WRIGHT-PATTERSON AIR FORCE BASE, OHIO 45433

81 8 18 179

NOTICE

This report has been reviewed by the Office of Public Affairs (ASD/PA) and is releasable to the National Technical Information Service (NTIS). At NTIS, it will be available to the general public, including foreign nations.

This technical report has been reviewed and is approved for publication.

William M. Roquemore

WILLIAM M. ROQUEMORE
Program Manager
Fuels Branch
Fuels and Lubrication Division

Arthur V. Churchill

ARTHUR V. CHURCHILL
Chief, Fuels Branch
Fuels and Lubrication Division

FOR THE COMMANDER

Robert D. Sherrill

ROBERT D. SHERRILL
Chief, Fuels and Lubrication Division

SECURITY CLASSIFICATION OF THIS PAGE (When Data Entered)

REPORT DOCUMENTATION PAGE

READ INSTRUCTIONS BEFORE COMPLETING FORM

1. REPORT NUMBER
AFWAL-TR-81-2018

2. GOVT ACCESSION NO.
AD-A103 023

3. RECIPIENT'S CATALOG NUMBER

4. TITLE (and Subtitle)
VELOCITY MEASUREMENTS IN CONFINED DUAL COAXIAL JETS BEHIND AN AXISYMMETRIC BLUFF BODY: ISOTHERMAL AND COMBUSTING FLOWS

5. TYPE OF REPORT & PERIOD COVERED
Interim Technical Report
1 JAN 79 — 30 SEPT 80

6. PERFORMING ORG. REPORT NUMBER
UDR-TR-80-90

7. AUTHOR(s)
Allan J. Lightman, Ph.D.
Peter D. Magill

8. CONTRACT OR GRANT NUMBER(s)
F33615-78-C-2005

9. PERFORMING ORGANIZATION NAME AND ADDRESS
University of Dayton
Research Institute
Dayton, Ohio 45469

10. PROGRAM ELEMENT, PROJECT, TASK AREA & WORK UNIT NUMBERS
304805 96

11. CONTROLLING OFFICE NAME AND ADDRESS
Aero Propulsion Lab (AFWAL/POSF)
Air Force Wright Aeronautical Lab.
Wright-Patterson Air Force Base, Ohio 45433

12. REPORT DATE
APRIL 1981

13. NUMBER OF PAGES
56

14. MONITORING AGENCY NAME & ADDRESS(if different from Controlling Office)

15. SECURITY CLASS. (of this report)
UNCLASSIFIED

15a. DECLASSIFICATION/DOWNGRADING SCHEDULE

16. DISTRIBUTION STATEMENT (of this Report)

Approved for public release; distribution unlimited

17. DISTRIBUTION STATEMENT (of the abstract entered in Block 20, if different from Report)

18. SUPPLEMENTARY NOTES

Submitted with UDR-TR-80-89

19. KEY WORDS (Continue on reverse side if necessary and identify by block number)

Laser Doppler Anemometer (LDA)
Free Jet
Bluff Body
Recirculating Flow
Combustion
Probability Density Function
Power Spectral Density
Mass Flow Computation

20. ABSTRACT (Continue on reverse side if necessary and identify by block number)

Measurements were made of the axial component of the flowfield in an Air Force combustion tunnel facility at Wright-Patterson Air Force Base. The tunnel is characterized by a bluff body, centered in the airflow duct, through which fuel can flow. The annular air flow around the centerbody creates a recirculation zone in the wake behind the bluff body. The recirculating flow interacts with the fuel jet and five distinct regimes of operation are delineated.

20. ABSTRACT (Continued)

Radial and axial profiles of the flowfield were made in isothermal and combusting flows. The free-jet behavior is that anticipated from other studies. A distinction from previous workers' data is the report herein of the existence of distinct modes in the velocity probability density functions. With both annular and fuel jets flowing, measurements were made of the fuel and air stagnation points along the centerline, in both isothermal and combusting flows.

FOREWORD

This interim report was prepared by the University of Dayton Research Institute (UDRI), Dayton, Ohio 45469 under Contract No. F33615-78-C-2005, Project No. 3048, Task 304805, Work Unit 96 with Dr. W. M. Roquemore (AFWAL/POSF) Government Project Monitor.

The report describes the laser Doppler anemometer (LDA) constructed for use with the combustor in Room 20, Building 18, Wright-Patterson Air Force Base. The LDA was used to measure axial velocities in both isothermal and combusting flows, under a variety of operating conditions. Velocity profiles were taken, radially and axially, and they are presented in this report. The computer interfacing and computer data processing software are described in an accompanying technical report.

This report concludes the effort on the one-dimensional measurement series. A new two-dimensional LDA will be constructed and utilized for measurements in the same combustion facility during the remainder of this program. This report covers the effort from January 1979 through September 1980.

The authors are Dr. Allan J. Lightman, Principal Investigator of this project, and Mr. Peter D. Magill. Project management is provided by Dr. E. H. Gerber. The contributions of Dr. W. M. Roquemore and Mr. R. Bradley (AFWAL/POSF) are gratefully acknowledged. Mr. C. Reeves (AFWAL/POSF) was especially helpful in the preparation of those graphs taken from the jointly authored AIAA publication. The Air Force personnel's assistance in conducting the experiments was most helpful. A special note of thanks is extended to Dr. L. Krishnamurthy (UDRI) whose understanding of the flow processes was invaluable. The assistance of Ms. P. Stewart, Ms. A. Cochran and Ms. R. Fannin in the preparation of this report is greatly appreciated.

TABLE OF CONTENTS

LIST OF ILLUSTRATIONS

LIST OF ILLUSTRATIONS (CONTINUED)

LIST OF ILLUSTRATIONS (CONTINUED)

LIST OF TABLES

NOMENCLATURE

a_s	air stagnation location
d	fuel tube diameter
D	centerbody diameter
f_D	Doppler frequency
f_s	fuel stagnation location
F_s	frequency shift
$\vec{k}$	propagation vector of laser light
L	fuel flow development length
r	radial position
R	duct radius
U	velocity in X direction $= \overline{U} + u$
$\vec{v}$	velocity vector $= U\hat{X} + V\hat{Y} + W\hat{Z}$
V	velocity in Y direction $= \overline{V} + v$
W	velocity in Z direction $= \overline{W} + w$
$\overline{W}_A$	average annulus velocity
W_F	fuel velocity
W_O	fuel velocity at entrance plane
X	horizontal coordinate normal to centerline
Y	vertical coordinate normal to centerline
Z	axial coordinate
Z_s	fuel stagnation location
λ	wavelength of laser light
$\bar{\ }$	the bar above a quantity indicates the time-averaged value while the lower case velocity designates the fluctuating component
$\hat{\ }$	designates a unit vector in the indicated direction

SECTION I

INTRODUCTION

1.1 OVERVIEW

The objective of this research was to measure the axial velocity flowfield in an Air Force combustion tunnel to provide data for model evaluation studies. The combustor is located in the Air Force Wright Aeronautical Laboratories, Aero Propulsion Laboratory (AFWAL/PO). The tunnel is characterized by a bluff body centered in the airflow duct. Fuel is injected from the center of the bluff body and air flows through the annular region. In combusting flow, the diffusion flame is stabilized by the recirculation region established in the wake of the centerbody. A description of the physical system is given in Paragraph 1.2.

A one-dimensional laser Doppler anemometer (LDA) system was constructed to probe the axial component of the flowfield velocity. It was mounted on a moveable table, and its probe volume could be traversed through the flowfield. The operation of the system was integrated into the Modcomp computer that is also used to monitor various combustor parameters. A description of the LDA apparatus is given in Section II. The computer controls and the data reduction and analysis programs are discussed in the accompanying Computer Software and Interfacing Report.[1]

Section III presents the results of the inlet conditions measurements. These measurements are a necessary starting point for any model of the flowfield. Measurements were made of the velocity decay in the fuel jet with a negligible annulus flow rate and are presented in Section IV. Section V contains the results obtained for annulus and fuel tube flowing, in isothermal and combusting flows. Flowfields for various operating conditions of the combustor are postulated in Section VI and the results of the experimental measurements are interpreted within that framework. Conclusions concerning the operation of the LDA apparatus are drawn in Section VII.

1.2 COMBUSTOR DESCRIPTION

The test section of the combustor, shown in Figure 1(a), consists of a cylindrical duct having a concentric centerbody with a flat end face. There are three viewing stations for optical access available from three sides at each station, through windows 7.62 cm X 30.48 cm. The centerbody face protrudes 5 cm into the field of view of the first window, permitting the LDA to approach the face as close as the LDA optics allow.

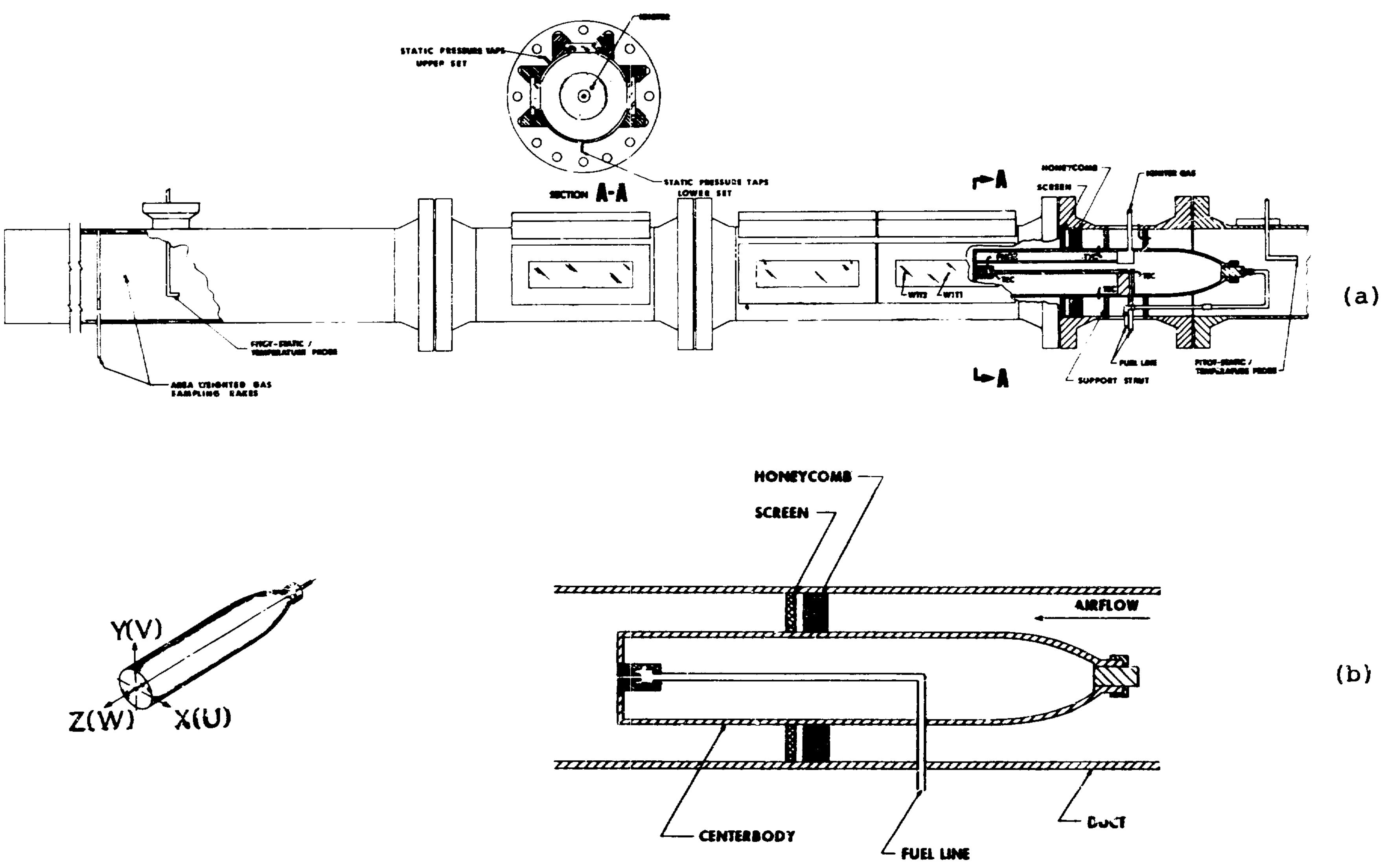

Figure 1. Schematic Diagrams of the Combustion Tunnel. (a) Total view with the upstream cutaway showing the centerbody extending into the first viewing station. A cross section (A-A) is drawn above. (b) Detail of the centerbody used. The reference coordinate system and velocity components (in parentheses) are shown on the left.

The window height limits the vertical scan possible when using the side windows. For axial scans there are zones where no signal can be recorded, such as between the windows. This serves to limit the range of variation of the inlet conditions while maintaining the region of interest at an accessible location.

Fuel is injected at the center of the centerbody face through a 4.8 mm diameter fuel tube, and air flows through the annular passage between the outer duct and the centerbody. The fuels used in this program were air and CO_2 in isothermal flow and C_3H_8 in combusting flow. Flow through the fuel tube is denoted "fuel" to distinguish it from the air flow in the annulus.

The centerbody is 14 cm in diameter and 79 cm long. The upstream surface of the centerbody is aerodynamically shaped to minimize disturbances in the annulus air flow. A 31.8-mm long square-cell honeycomb flow straightener, with cell size 4.8 mm x 4.8 mm, and two number 16 mesh screens are mounted in the annulus. The inside diameter of the duct is 25.[illegible] cm. The centerbody shown in Figure 1(a) has been modified to accept other fuel tubes and the new face is shown in Figure 1(b).

SECTION II

LASER DOPPLER ANEMOMETER

The operating principle of the LDA system is the linear relationship between the velocity of a scattering site and the Doppler frequency generated. This is covered in detail in many publications, for instance Durst, et al.[2]

2.1 OPTICAL SUBSYSTEM

The optical arrangement used in this study is that of the differential Doppler system. Two optical beams, monochromatic and in phase, are crossed at the region of interest. The Doppler shifted light scattered from the two beams is heterodyned and the resulting Doppler frequency is independent of the directions of the individual input beams, depending instead on the difference in their wave vectors. If the input beam wave vectors are $\vec{k}_1$ and $\vec{k}_2$ ($|\vec{k}| = 2\pi/\lambda$), as shown in Figure 2, the resulting Doppler signal is

$$f_D = (\vec{k}_1 - \vec{k}_2)\cdot\vec{v} \tag{1}$$

If $|\vec{k}_1| = |\vec{k}_2|$, as it is when both beams are derived from the same laser, their difference $(\vec{k}_1 - \vec{k}_2) = \vec{k}$ is aligned perpendicular to the bisector of the angle they form. Thus, the Doppler frequency produced is directly proportional to the velocity ($v_\perp$) of the scattering site perpendicular to the bisector. To get information on other directions of motion, it is necessary to utilize other LDA systems aligned for the directions desired.

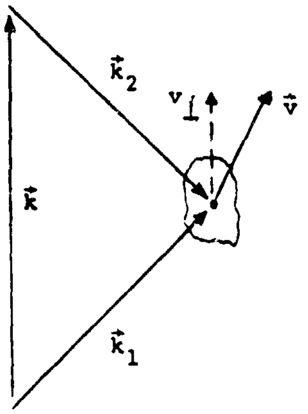

Figure 2. Incoming Laser Beams with Wave Vectors $\vec{k}_1$ and $\vec{k}_2$, Scatter from the Particle Shown and the Doppler Signal Produced is a Measure of $v_\perp$.

The actual physical layout of the equipment is shown in Figure 3 with the optics detailed in Figure 3(a) and the electronics in Figure 3(b). The argon ion laser operates at 514.5 nm. The beam is passed through a spatial filter and beam expander combination. The spatial filter ensures that the light is a clean Gaussian TEM_{00} beam with no higher order modes to modulate the signal and create interferences. The beam expander accomplishes two things. First, it expands the beam ($\simeq 2x$) so that the focussed volume in the combustor is smaller. Second, by adjustment of the collimating lens, it ensures that the laser beams cross at their waists. This minimizes the interrogation volume and ensures that the Doppler frequency generated is uniform throughout the volume.

The pentaprism deflects the beam 90° into a symmetric beamsplitter with a 50-mm beam separation. An acousto-optic Bragg cell shifts one laser beam 40 MHz in frequency from the other so that directional ambiguity is eliminated. The directional ambiguity results from the fact that the signal processor, which measures the Doppler period, cannot differentiate between the period due to the frequency $\vec{k} \cdot \vec{v}$ from $\vec{k} \cdot (-\vec{v})$. By adding a shift frequency, F_s, the directionally opposed scattered signals yield frequencies $F_s + \vec{k} \cdot \vec{v}$ and $F_s - \vec{k} \cdot \vec{v}$. Provided $F_s > (\vec{k} \cdot \vec{v})_{max}$, the directions are resolved. A compensator is used in the reference beam path to ensure that both beams travel the same optical path length and remain in phase.

Some additional optics are needed to ensure that the beam intensities are equal and that they cross properly after passing through the focusing lens (f = 381 mm). The forward scattered radiation is collected by a spherical mirror (f = 280 mm) and, due to space restrictions, it is returned through the combustor unfocused. The light is focused by the lens used to cross the input beams, deflected by a mirror sitting between the input beams, and passed to a multiplier phototube (MPT), usually through a laser line filter and a pinhole filter. The last two items serve respectively to remove extraneous radiation coming from the flame and to limit the field of view of the detector.

The system was constructed to withstand the expected acoustic and thermal environments in the test facility. The signal is obtained by scattering from titanium dioxide particles introduced both upstream of the centerbody and into the fuel line through fluidized-bed seeders. The seeder designs are similar to that described in Reference 3. With the Bragg cell modulator turned off, the measurement volume (spot) is an ellipsoid measuring 75 μm in diameter by 250 μm in the forward (optical) direction. However, when the modulator is turned on, the spot is distorted and the ellipsoid measures

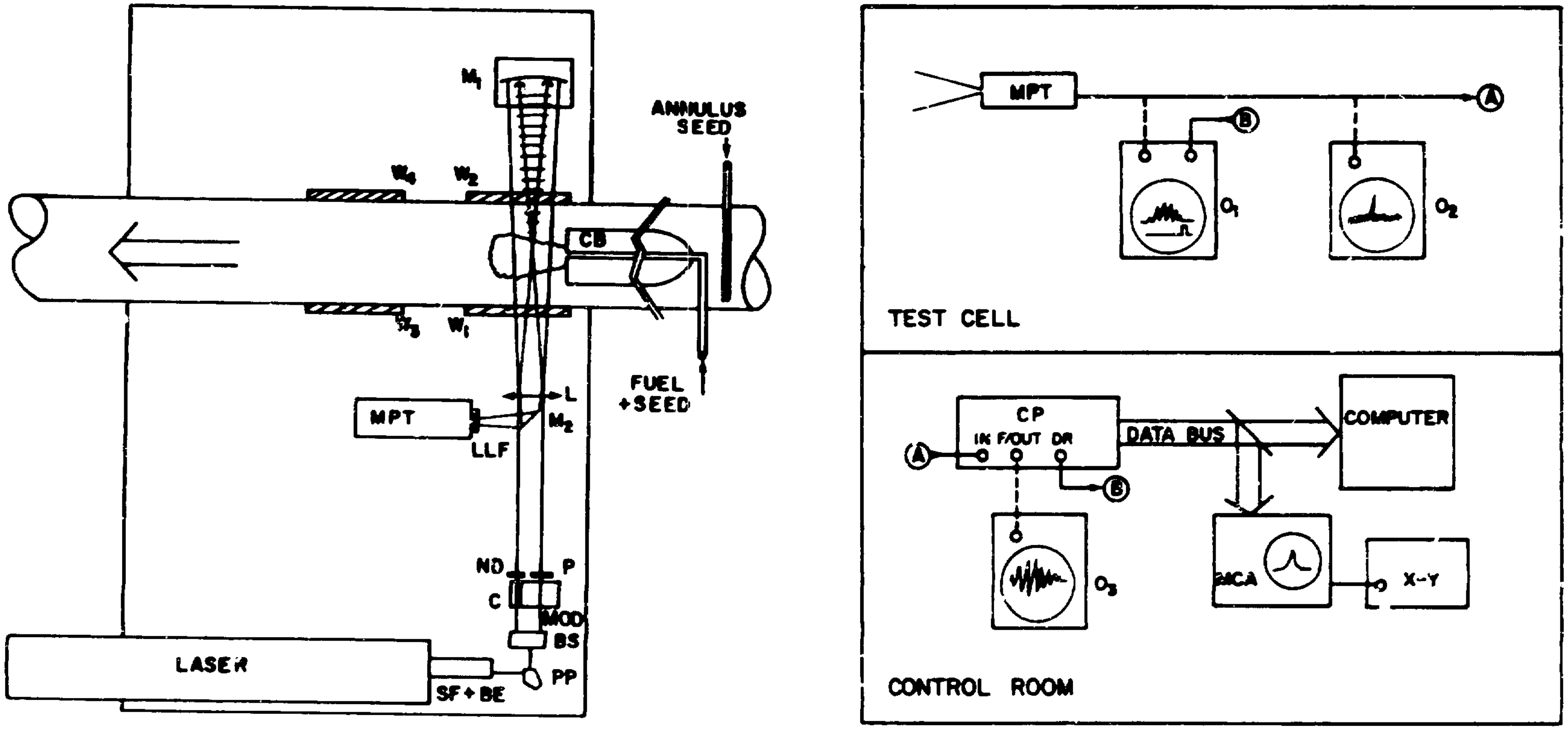

(a)

(b)

Figure 3. One-Dimensional LDA System. (a) Optical layout. SF+BE: spatial filter and beam expander. PP: pentaprism. BS: beamsplitter. MOD: modulator. C: compensator. P: beam steering prism. ND: neutral density filter. L: lens. M_i: mirrors. LLF: laser line filter. MPT: multiplier phototube detector. W_i: tunnel access windows. CB: combustor centerbody. (b) Electrical signal paths. MPT: multiplier phototube. O_1: oscilloscope displaying real-time scattering signal and valid data signal (B). O_2: spectrum analyzer. CP: counter processor. O_3: fast storage oscilloscope for examining filtered scattered signal. MCA: multi-channel analyzer. X-Y: recorder.

150 μm by 250 μm in cross section and 1.5 mm in length. The region of interest is scanned by moving the entire optical bed, with all components remaining rigidly fixed.

2.2 ELECTRONIC SUBSYSTEM

The scattered Doppler signal is processed by a counter processor. In the present design the frequency range of the signal is limited from approximately 10 to 50 MHz corresponding to a velocity range of +120 m/s to -40 m/s respectively. The processor has a feature allowing selection of the number of cycles in the Doppler burst. Sixteen cycles are used to restrict data to that obtained near the center of the scattering volume.

In the electronic processing system shown in Figure 3(b), the detector is connected to the processor through 30 meters of coaxial cable. The alignment oscilloscope and spectrum analyzer are disconnected during experiments so that the cable is continuous and properly terminated to prevent reflections. Cable loss is minor at all frequencies of interest (Figure 4). The multichannel analyzer proved essential during alignment and in setting amplifier gains, etc. Signal distortions, gain broadening, and gain frequency-shift effects were readily visible so that amplifier gain, laser power, and MPT voltage could be adjusted below the level where signals become distorted by too high a gain. In practice the MPT voltage and laser power were left fixed and only the amplifier gain was adjusted.

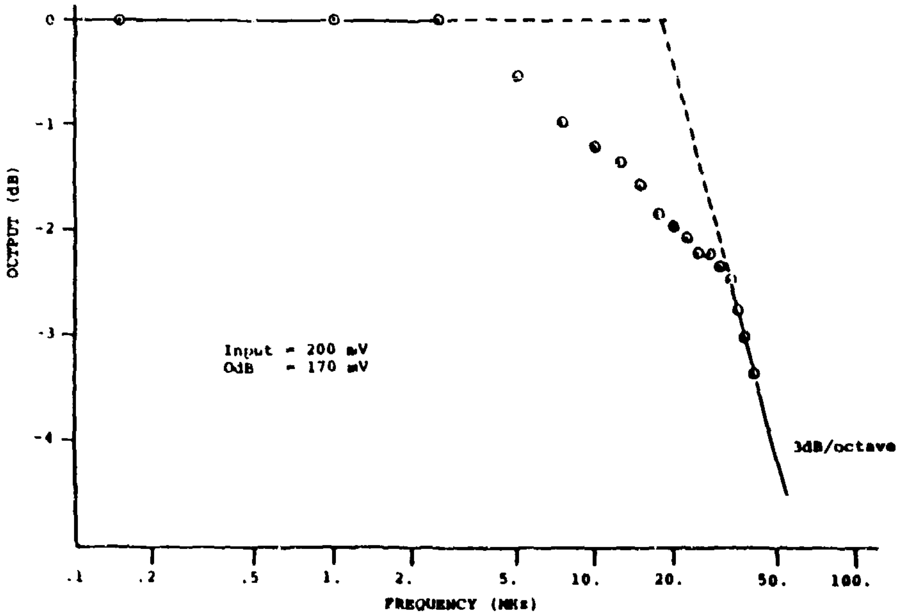

Figure 4. Transmission Characteristics for Cable Carrying Detected Doppler Signal from Test Cell to Control Room.

2.3 MEASUREMENT CONSIDERATIONS

The LDA system was checked against measurements made by Pitot-static and hot-film probes. As both of these instruments are accurate only in nonrecirculating and low-turbulence flows, the comparisons were made in the annular flow near the entrance plane with the Pitot tube and in the fuel jet (with no annular air flowing) with the hot film. The hot-film probe was profiled through the jet and both the velocity and turbulence level were monitored. The agreement of the LDA measurements and those made with the conventional probes was within the anticipated accuracy of 1 percent at low turbulence levels and within 5 to 10 percent at higher turbulence levels.

In a recirculation zone, the direction of flow at a given location can change with time. The use of individual realization LDA instruments to measure average velocity in multifluid-mixing regions may result in biased data if the seed density in each flow is not properly adjusted. The average velocity is biased in favor of the velocity in the flow direction containing the highest number of seed particles. In practice, it is very difficult to equalize the seeding densities in two separate streams for mixing region measurements, and no concerted attempt was made to do so in the present study. Instead, the extreme variations in the results were determined by the use of first one seeder exclusively and then the other. The results show changes when conditioned by seeding only one of the flow streams, but the changes are not substantial in that the fuel stagnation points move ±1 cm, and the air stagnation points show no effect. Also, the velocity profiles remain similar even in the most adverse seeding conditions. However, the absolute value of the mean velocity can change substantially for certain conditions such as combusting flows near the fuel stagnation point. The precision of the velocity data is typically better than 10 percent except near stagnation points where a change in velocity of a few meters per second can result in a very large percentage error. Careful studies are needed to examine the possible effects of velocity biasing due to differences in seed densities in flows coming from different directions.

SECTION III

ENTRANCE FLOWFIELDS

Predictive studies require the entrance conditions as boundary values in the numerical modeling. These values were measured both for the annulus and for several fuel tubes, under a variety of flow conditions. The measurements also served as a check of the LDA accuracy by computation of the mass flux and comparison with the mass flowmeter readings. This comparison is made with the tunnel measurement in which there is the highest degree of confidence and thus provides the best test.

3.1 ANNULUS MEASUREMENTS

In the annulus measurements the LDA apparatus was positioned 1 mm upstream of the centerbody face. Sufficient scattering was intercepted by the collection mirror to permit radial scans to within 1 mm of the centerbody. At this point surface scattering and shadowing created a sufficient background to make the signal uninterpretable. At the outside boundary, the window, interference was more severe and the closest approach was limited to within 5 mm. The seed particles and dirt adhered to the window and strongly scattered the incident light. The detector could not see the weaker signal intensity in the presence of this background. An effort was made to clean the windows and then run, but the windows became dirty with the first puff of annulus air. A window flush was tried but this disturbed the flowfield in the measurement region. As a result, measurements were not obtained up to the boundary.

The LDA results for velocity and turbulence intensity as a function of radial position are shown in Figures 5 and 6, respectively. Measurements were made at four flow conditions, 0.5, 1.0, 1.5, and 2.0 kg/s corresponding to the range of normal operating conditions. To compute the mass balance, the profiles were extended to within 0.5 mm of the boundaries using a best guess continuation. In the last 0.5 mm it was assumed that the velocity went to zero linearly. The boundary region is small and its contribution to the mass flux is insignificant. The results of this computation are given in Table 1. All computations exceed the venturi flow measurements by 3 to 4 percent. The agreement was considered satisfactory and gave confidence in the LDA measurements. The discrepancy is small but consistently positive, suggesting that there is a calibration error. This could be in the venturi calibration, in the calibration of the LDA's frequency-to-velocity conversion factor (it is difficult to measure this factor to better than 2 percent), in the LDA

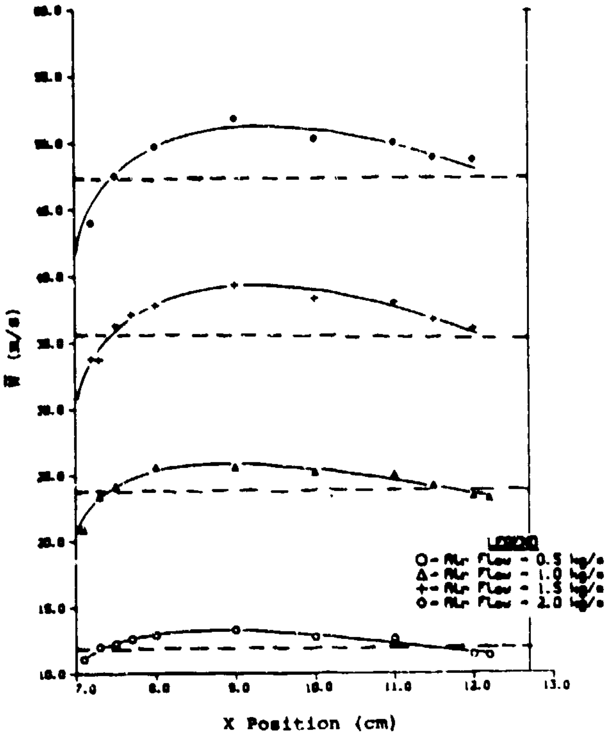

Note that in this and all following graphs the solid curves are for illustration only, unless noted otherwise, and do not correspond to any theoretical formulation.

Figure 5. Average Velocity Profiles Measured in the Annulus Upstream of the Bluff-Body Face for Four Flow Conditions. The centerbody surface is at x = 7 cm, and the duct window is at x = 12.7 cm. The dotted lines are the mass averaged velocity in the annulus.

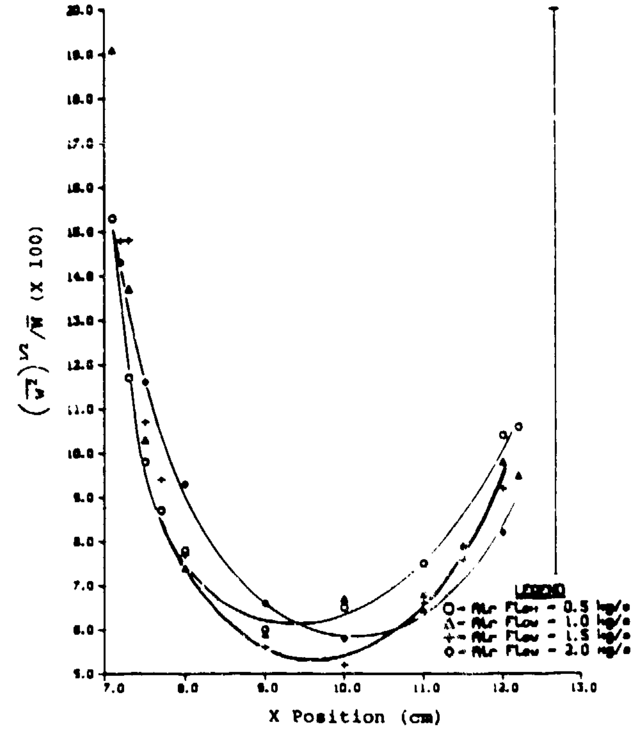

Figure 6. Turbulence Intensities Measured in the Annulus Upstream of the Bluff-Body Face at Four Flow Conditions. The annulus extends from x = 7 cm to x = 12.7 cm. The solid curves show the radially outward motion, with increasing air flow, of the location of the minimum turbulence intensity.

measurement volume positioning, in the temperature (density) measurement, or in any number of other sources. The agreement was considered sufficient and no further effort was expended to improve it.

TABLE 1
VELOCITY MEASUREMENTS OBSERVED IN ANNULUS
1 mm UPSTREAM OF CENTERBODY FACE

Mass Flowmeter (kg/s)	Computed Mass Flux (kg/s)
0.50 (±0.02)	0.52
1.00 (±0.02)	1.03
1.50 (±0.03)	1.56
2.00 (±0.04)	2.07

Two observations should be made from Figures 5 and 6: (a) the annulus flowfield velocity is not constant and shows the influence of the centerbody, the velocity field curvature becoming more pronounced at higher mass fluxes; and, (b) the turbulence intensity does not go below 5 percent and there is a substantial increase at the boundaries.

The measured values reported here were usually obtained from a distribution of 2,000 samples. It was determined (Appendix A) that this number of samples was sufficient to ensure that the variables of interest: average value, standard deviation, skewness, and kurtosis, had stabilized.

3.2 FUEL TUBE STUDIES

Three fuel tubes were investigated in this program. Two have diameters of 4.78 mm and length-to-diameter ratios (L/d) of 1 and 15. They will be referred to as the short taper (ST) and 'regular' tubes respectively. The third fuel tube has a diameter of 4.50 mm and an L/d of 80. The ST tube was designed to produce a flat-top velocity profile. The 4.50-mm tube has a sufficiently long L/d that the flow in the tube is fully developed at the combustor entrance plane. The 'regular' tube is so called because it was used most often. Its L/d resulted in the entrance flow being characteristic of a flow-development-transition region.

The LDA instrument was used to profile the entrance planes of the nozzles in situ. As a result of the shadowing effect of the centerbody, the closest axial approach to the entrance plane that could be achieved was 4 mm downstream. The profiles shown were measured at this location. The scans were taken in the Y (vertical) direction because the LDA measurement spot is an ellipsoid with axes of approximately 1.5 mm in the X direction and 0.15 mm in the Y direction. When the instrumental profile is taken into account (see Appendix B) the X profile will be considerably distorted. The Y profile will be affected at the edges of the flow only and a correction can be made more easily.

Fuel tube profiles were taken for the 4.78-mm tubes with CO_2 as the fuel, at flow rates of 4 and 8 kg/hr, with little or no air flowing in the annulus. Lack of time precluded the measurement of the 4.50-mm fuel tube with CO_2 as a fuel, so a previous measurement with air as the fuel at 5 kg/hr is included. The results have been normalized to the centerline velocity (W_0) and the two sets of measurements for the two flow rates for each 4.78-mm tube are overlayed. The results are similar for each flow through a particular tube so that the velocities scale linearly with the mass flux. Computed mass flows for these profiles agree with flowmeter readings to within 25 percent. If a correction is applied to account for instrumental broadening, the agreement is within 5 to 10 percent. The mass flux is extremely sensitive to the contributions at the edges (due to the large area), and small changes in velocity produce substantial mass flux changes. Since the fuel tubes are so small (radius < 2.5 mm), even the Y cross section of the LDA spot is too large (0.15 mm) to produce a suitable profile, one yielding a mass flux comparison better than 5 to 10 percent. If velocity profiles are to be studied in more detail, a microscopic LDA volume will be required and the fuel tubes will have to be operated outside the tunnel. This change would permit the LDA to approach closer than 4 mm and eliminate the possibility that entrainment is increasing the mass flux.

The similarity profiles of the velocity for the 'regular,' ST, and 4.50-mm fuel tubes are shown in Figure 7. The turbulence intensities for these tubes are shown in Figure 8. Figure 7(b) shows the flat-top structure desired for the ST fuel tube, extending over 80 percent of the diameter. The corresponding turbulence intensities, Figure 8(b), are low (<4 percent) across most of the tube. The 'regular' fuel tube experimental details indicate higher turbulence intensities in the flow at the fuel tube edge and a more limited region of low turbulence intensity (≈60 percent of the diameter) than for the ST fuel tube, as seen in Figure 8(a). This point is, for now, the only difference in the entrance profiles of the 'regular' fuel tube compared with the ST fuel tube. In the next section it will be shown that downstream measurements of the velocity probability density functions (pdf's) are markedly different for the 'regular' tube compared with the other two.

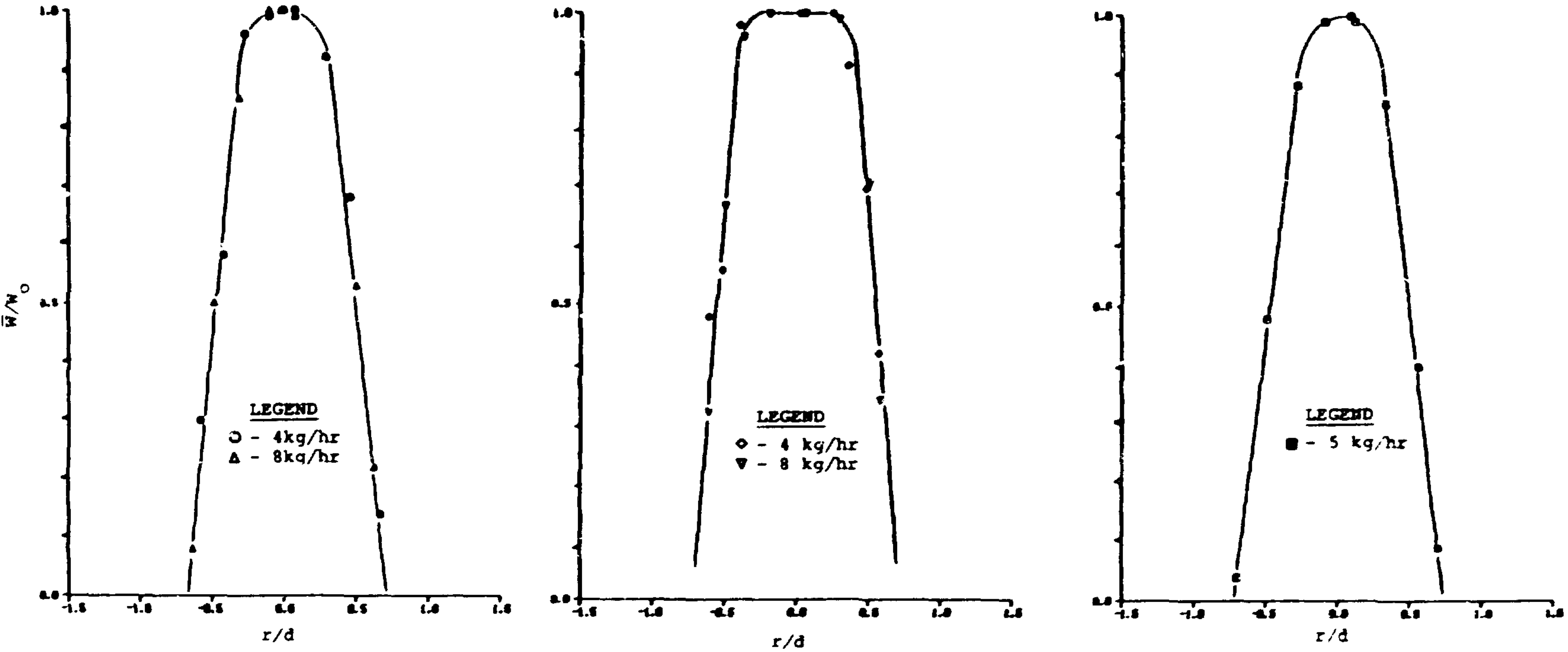

(a) (b) (c)

Figure 7. Entrance Profiles Observed Normalized to the Centerline Velocity (W_o) for the (a) 'Regular' Fuel Tube with CO_2 as Fuel, (b) ST Fuel Tube Showing the Flat-Top Profile with CO_2 as Fuel, and (c) 4.50-mm Fuel Tube with Air as Fuel.

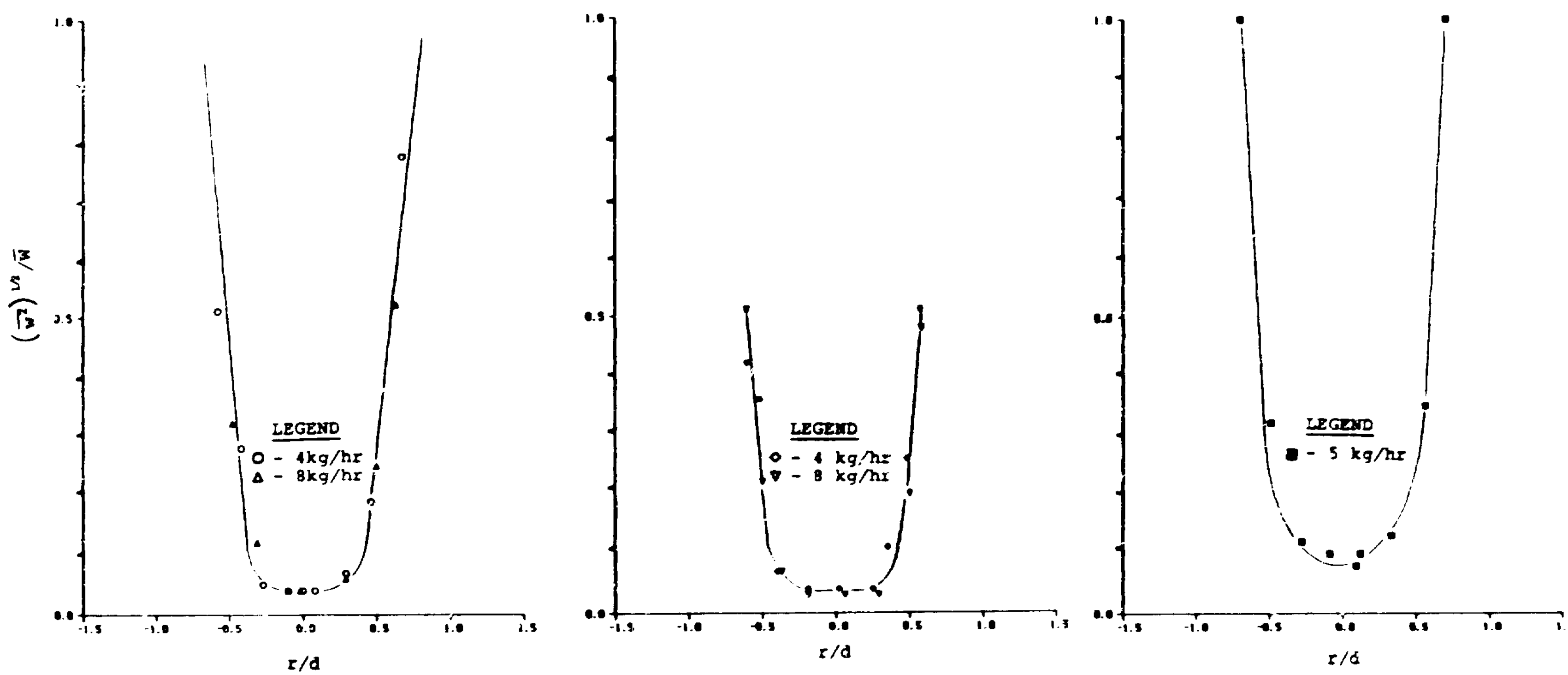

(a) (b) (c)

Figure 8. Turbulence Intensity Measurements Corresponding to the Velocity Measurements in Figure 7 for the (a) "Regular" Fuel Tube, (b) ST Fuel Tube, and (c) 4.50-mm Fuel Tube.

The entrance profiles for the 'regular' tube were also measured with annulus flows of 1.0 and 2.0 kg/s, at 4 and 8 kg/hr CO_2 fuel flow. The velocity profiles, normalized to the centerline velocity (W_0), and the turbulence intensities are shown in Figures 9 and 10 respectively. The annular flow around the centerbody sets up a recirculation zone and a reverse flow jet opposing the fuel flow (Section VI). If this jet is strong enough it can affect the fuel tube profile, as seen by a spreading of the fuel jet. The peak velocity is also reduced but this is not observable on a normalized plot. The turbulence intensities are also affected, shown by a broadening of the region with higher turbulence (at the edge of the fuel tube). Also, at a fuel flow of 4 kg/hr with an annulus flow of 2 kg/s, the centerline turbulence intensity increases sharply. In this last case a plot of w would have been almost constant across the tube.

Earlier in this section it was stated that the existence of similarity profiles indicates a linear variation of velocity with mass flux. This fact was used as a calibration check. The LDA measurement volume was positioned on centerline in front of the fuel tube, and velocities were measured as a function of mass flow. This relation is linear and the slope repeats (Figure 11). It was noted that there was a departure from linearity at 120 m/s. After considerable effort this was traced back to the processor's front end filters (Appendix C). At 120 m/s the signal pedestal produces harmonics that are sufficiently high in frequency to be passed by the high-pass filter. These higher harmonics are then processed as a Doppler burst and their period is similar to the period the real signal produces when downshifted from the Bragg cell reference. As a result, the signal interpretation is ambiguous and reliable measurements could not be made. The optical and electronic system will be modified during the next phase of this program to overcome these problems.

In an effort to characterize the fuel tube flowfield, a computer analysis was made of the spectral content of the velocity history measured in front of the fuel tube. This was done by taking the autocorrelation function of the velocity history and then Fourier transforming, following the technique of Mayo, et al.[4] A representative power spectral density is shown in Figure 12. The contribution around 250 Hz occurs for each fuel tube. Outside the potential core, downstream, this feature either disappears or is washed out behind a broad spectral structure. The 250 Hz feature also shows up in power spectral densities computed for annulus data taken at the entrance. This interesting feature will be investigated in the future studies.

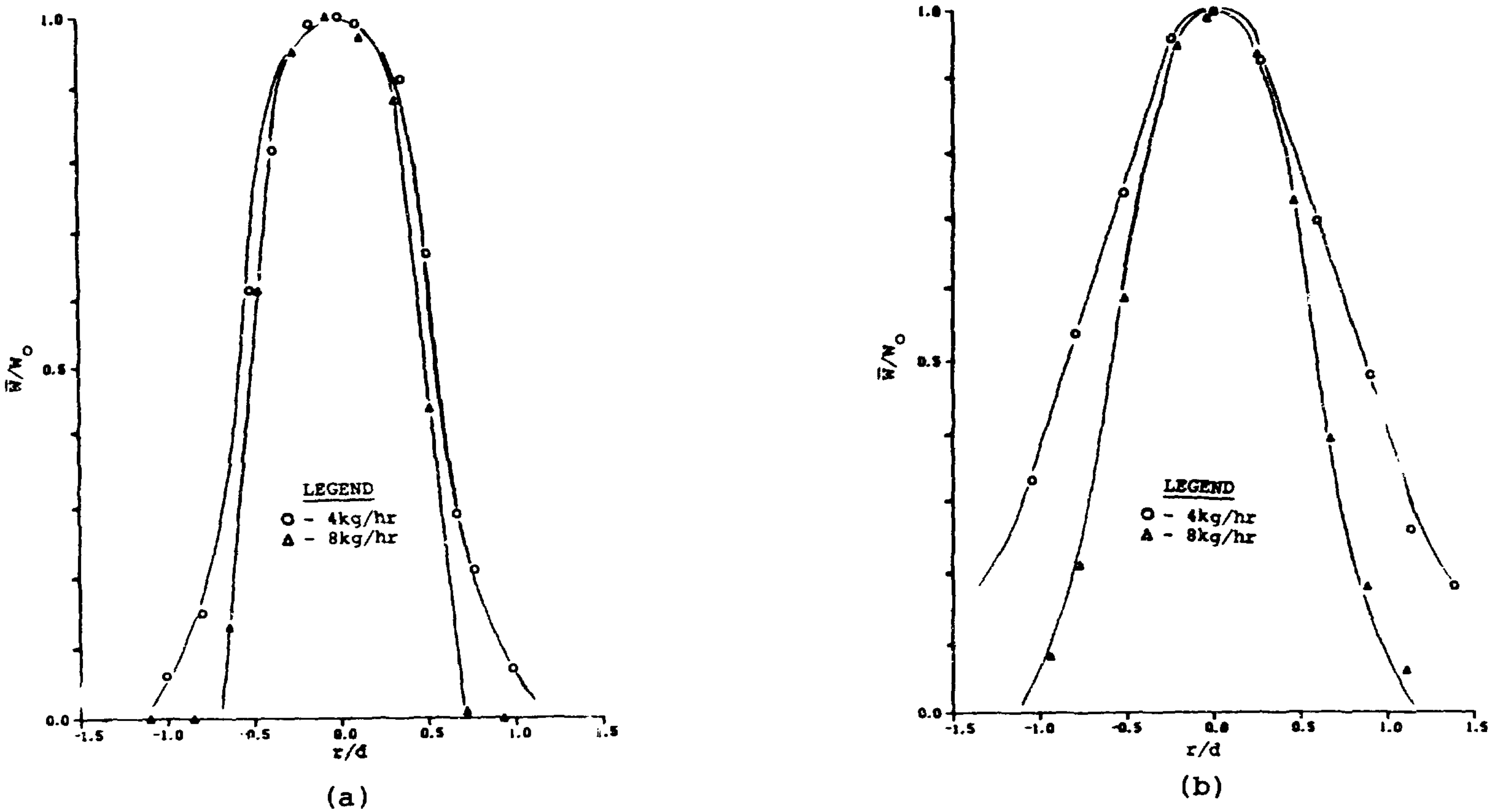

(a)

(b)

Figure 9. Normalized Velocity Profiles, Measured at Z = 4 mm, of Regular Fuel Tube with (a) 1 kg/s and (b) 2 kg/s of Annular Air Flowing.

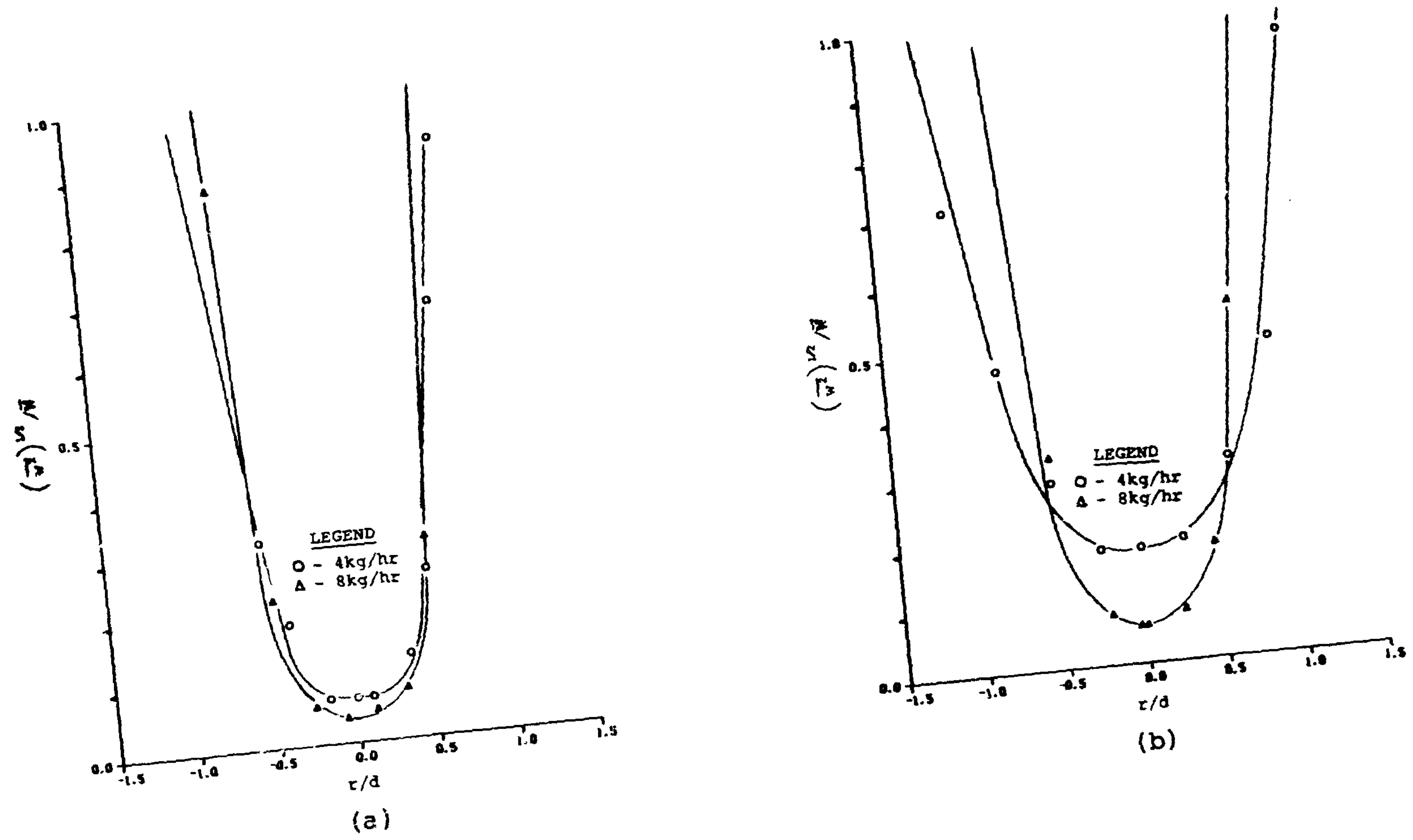

Figure 10. Turbulence Intensity Profiles, Measured at Z = 4 mm, of the Regular Fuel Tube with (a) 1 kg/s and (b) 2 kg/s of Annular Air Flowing.

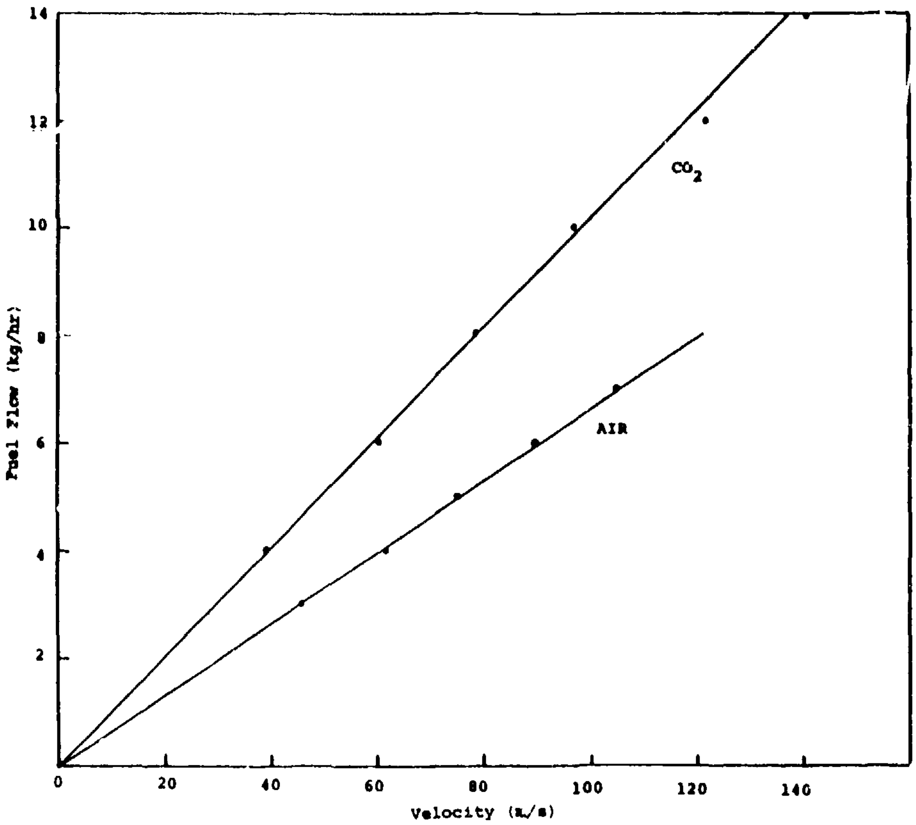

Figure 11. Plot of Mass Flow Rate versus Centerline Velocity from the Regular Fuel Tube. The linearity demonstrates the self-similarity of the inlet profiles at all flow rates. The ratio of the slopes of the two curves equals the ratio of the densities of the fuels (CO_2, air).

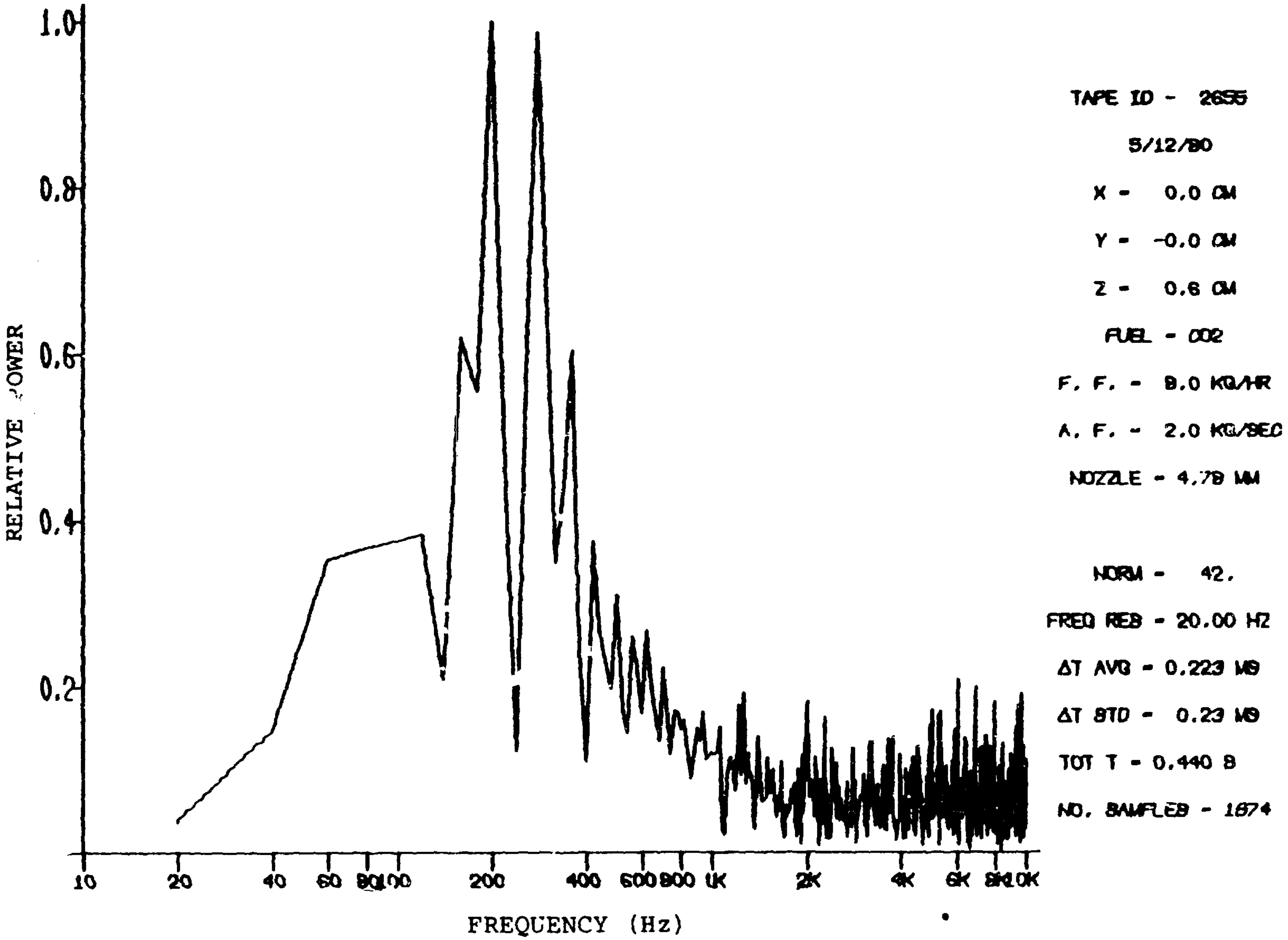

Figure 12. Power Spectral Density taken on Centerline Z = 4 mm, 8 kg/hr CO_2 Flowing through the Regular Fuel Tube, with Annular Flow of 2 kg/s.

SECTION IV
FREE JET MEASUREMENTS

Measurements were made of the axial velocity as a function of axial position along the centerline to characterize the fuel tube performance in the duct. It was expected that all the fuel tubes (described in Section III) should show the traditional free jet decay in velocity outside the potential core. The expected behavior is

$$W/W_o \propto d/Z \qquad (2)$$

where W is the axial component of velocity, measured at Z, W_o is the value of W at the entrance, and d is the fuel tube diameter.

An extensive study of the literature has been compiled by Harsha.[5] The free jet decay consistently shows the dependence in equation (2). Typically the data are plotted as log (W/W_o) versus log (Z/d) with a slope of -1. The knee position varies considerably in the data shown while its distribution appears to be within the limits $5 < Z/d < 10$

Witze[6] has stated that the free jet decay dependence should have the form

$$W/W_o = 1 - \exp(\alpha/(1-Z/Z_c)) \qquad Z>Z_c \qquad (3)$$

$$= 1 - \exp(A/(B-Z/d)) \qquad (4)$$

where α, Z_c, A, and B are constants that can be evaluated from the measured results. For $Z/d >> A, B$

$$W/W_o \simeq A(d/Z) \qquad (5)$$

---

*This variation may be the result of the Mach number dependence of the flow or the inlet profile conditioning as prepared by the various researchers whose data are used. In the data presented here the inlet profiles show substantial variation, yet the data can be reduced to a single curve.

For free jet decay in this regime Pai[7] has evaluated the dependence with the result $A = 6.5$.

The results of the measurements of the velocity for the three fuel tubes available, with fuel flows of 4 and 8 kg/hr of CO_2 through each, are shown in Figure 13. The data have been fit to Equation (4) with the result

$$W/W_o = 1 - \exp(7.5/(6.5 - Z/d)) \qquad (6)$$

This result is shown as the solid curve in Figure 13. The parameters have been evaluated to be $A = 7.5 \pm 5\%$ and $B = 6.5 \pm 10\%$. Thus the result is different from that obtained by Pai[7] or that of Lau, et al.[8] who obtained $A = 6.5$ for a free jet at a Mach number of 0.28, but it appears to be within experimental errors. A much more detailed study is necessary to ascertain if the discrepancy is real.

The turbulence intensities for the three fuel tubes and two flow conditions, (Figure 14), also show the traditional behavior.[9] The turbulence intensity remains low in the potential core, rises in the transition region, and then peaks at about 23 percent when the flow has become fully developed. The results for each fuel tube appear to be consistent, with no individual trends clearly evident. This belies the fact that there is, in fact, a substantial difference in the properties of the flowfields of the fuel tubes. This can best be seen when the probability density functions for the measurements at each location are examined.

Figures 15 and 16 show the pdf's for the 'regular' fuel tube and the 4.50-mm fuel tube, respectively, measured at the same downstream locations. The plots have a logarithmic vertical scale, severely compressing the result. The differences are more dramatic on a linear plot, as seen in Figures 17 and 18. Both the ST and the 4.50-mm fuel tubes give the same shape pdf's at each normalized location. The 'regular' fuel tube shows the existence of discrete structures in the pdf. These structures appear in the transition region of the flowfield and fade away as the flow becomes fully developed. It is now thought that the emergence of these structures may be a result of the inlet profile of the 'regular' fuel tube (Section III), as this is the only difference observed in the experimental conditions between the runs. More detailed conclusions will have to await further study.

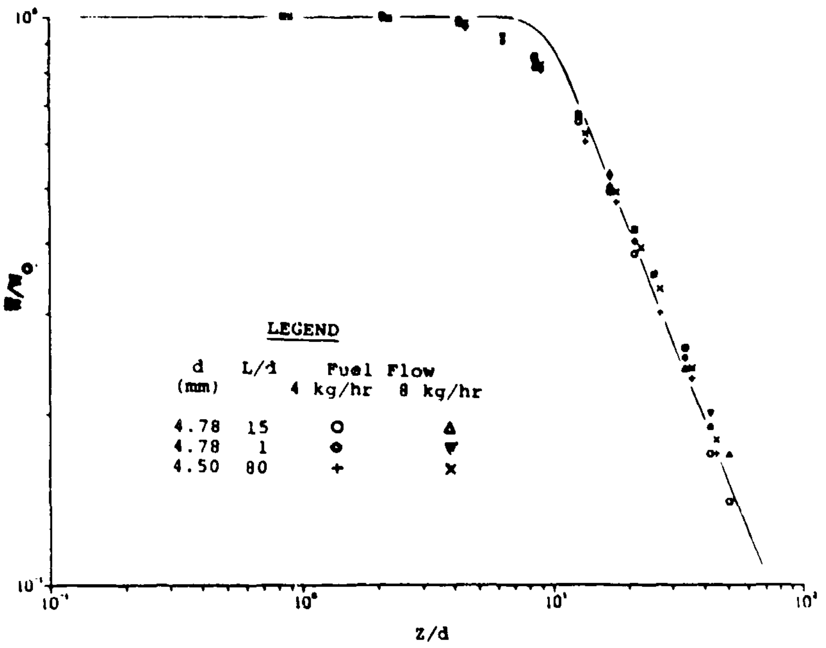

Figure 13. Decay of Centerline Velocity Normalized to the Velocity Measured at Z = 4 mm (W_0). The solid curve is the fit of the data to the formulation of Witze. (See Reference 6.)

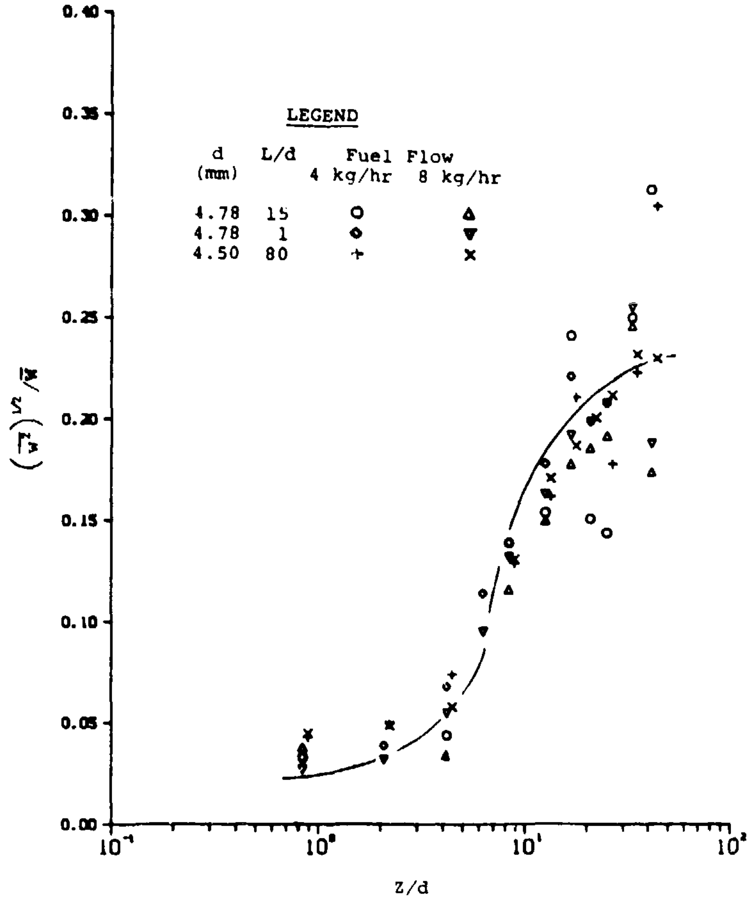

Figure 14. Turbulence Intensity Profiles along the Centerline. The solid curve is taken from data given for similar flow conditions. (See Reference 9.)

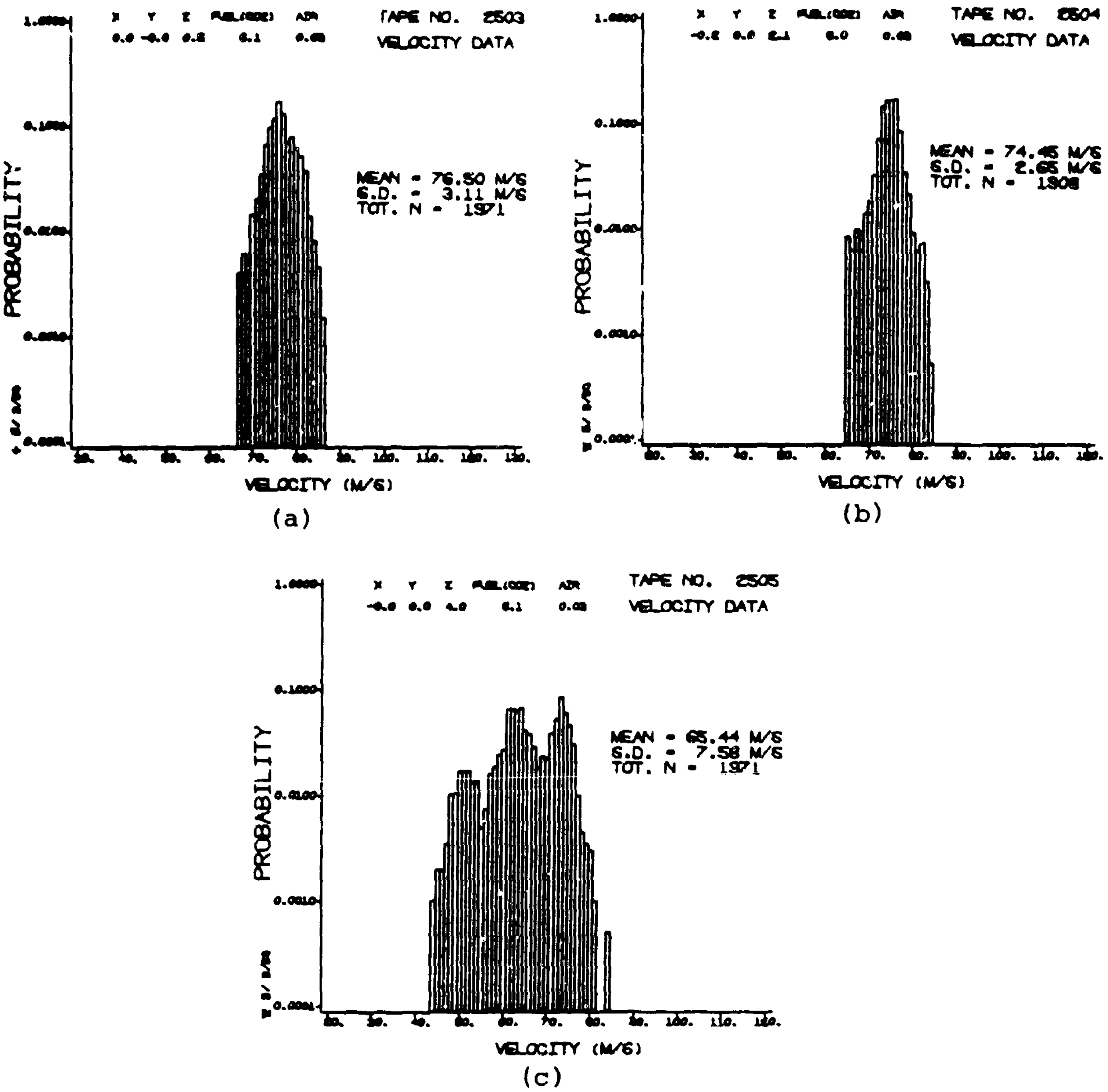

(a)

(b)

(c)

Figure 15. Probability Density Functions for Centerline Velocity Measurements Observed Downstream from the 4.78-mm L/d = 15 Fuel Tube. The distributions were measured at Z = (a) 0.5 cm; (b) 2 cm; (c) 4 cm. Note that the vertical scale is logarithmic.

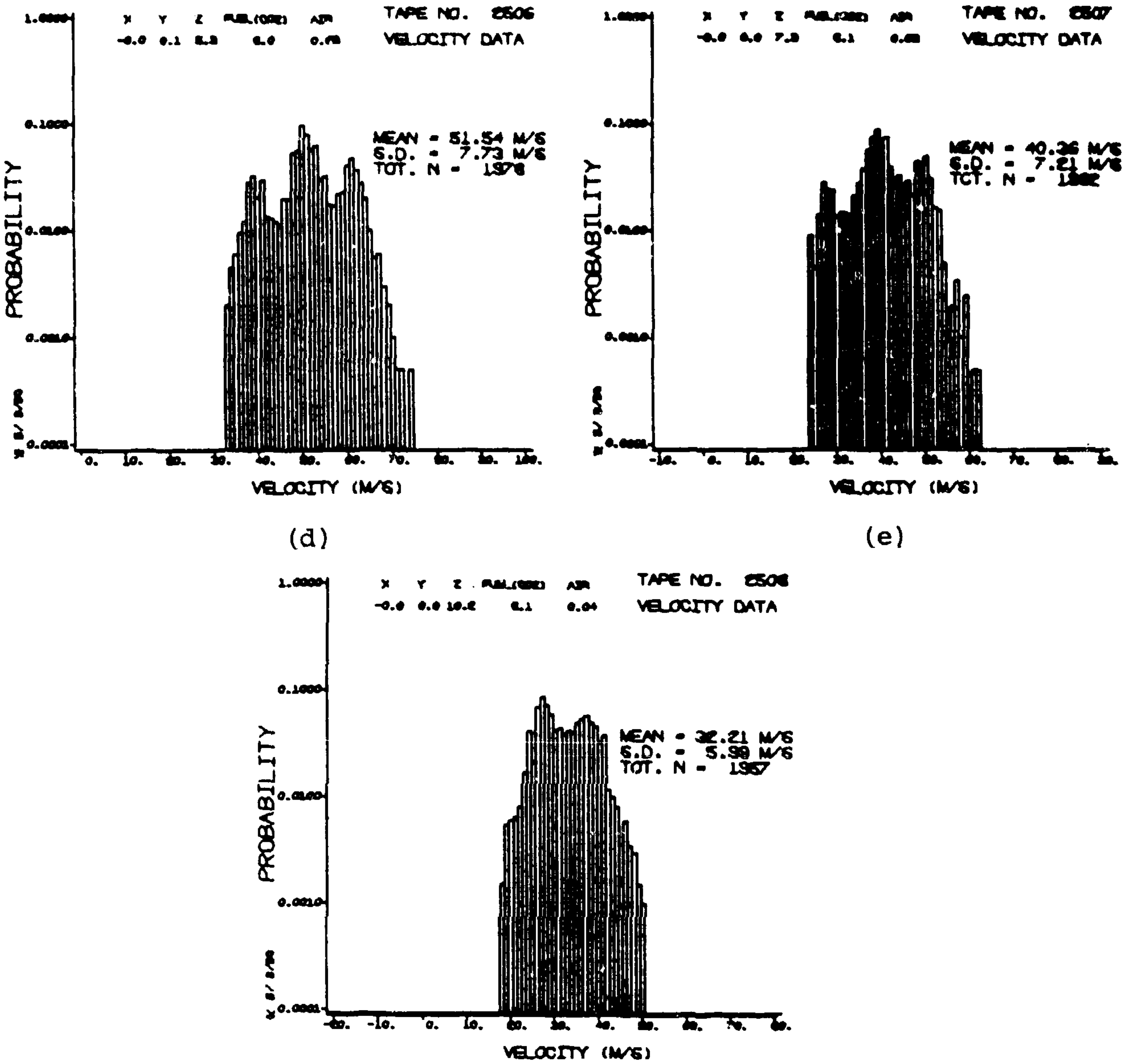

(d)

(e)

(f)

Figure 15. (continued) Probability Density Functions for Centerline Velocity Measurements Observed Downstream from the 4.78-mm L/d = 15 Fuel Tube. The distributions were measured at Z = (d) 6 cm; (e) 8 cm; (f) 10 cm. Note that the vertical scale is logarithmic.

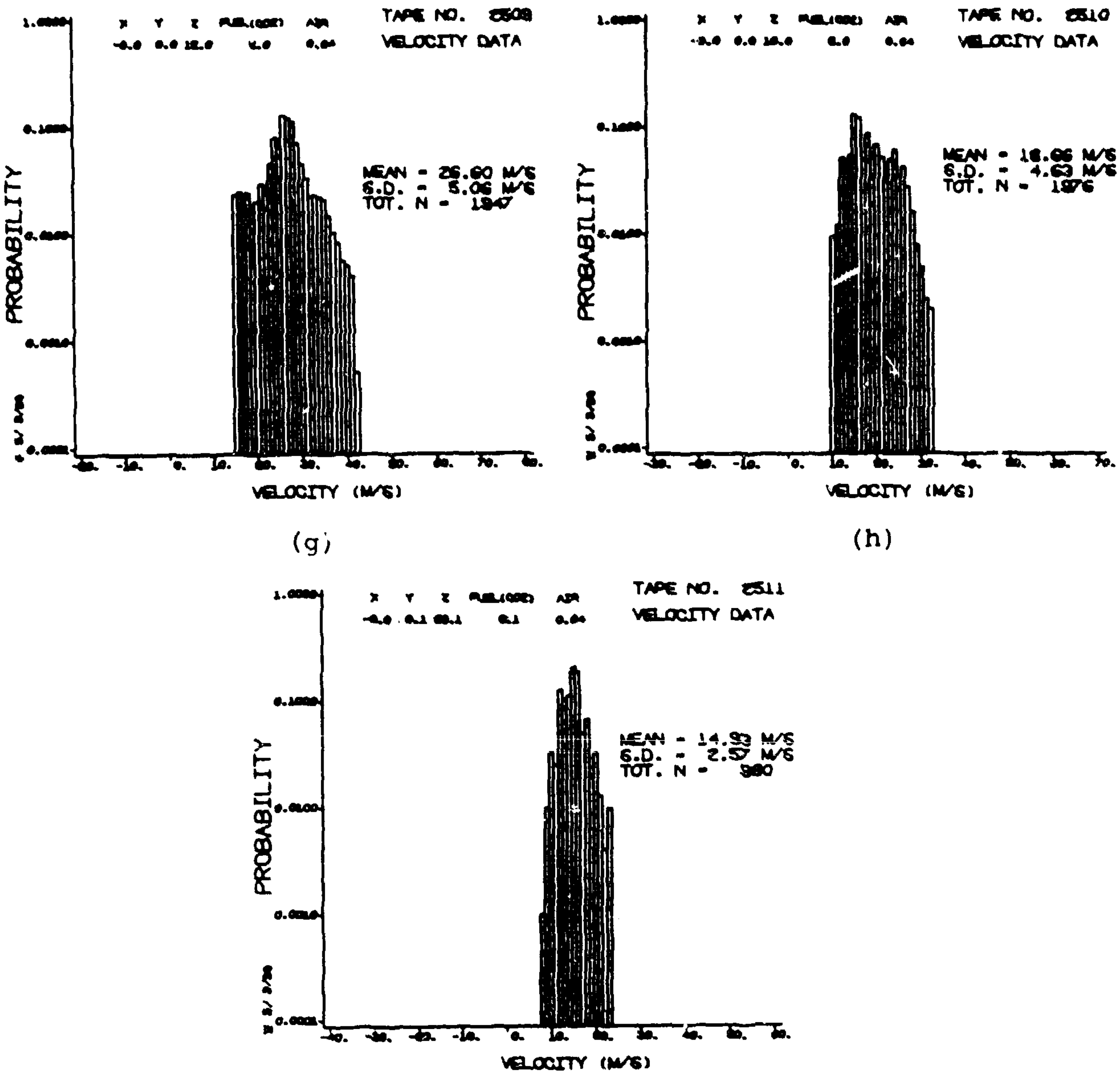

(g) (h)

(i)

Figure 15. (continued) Probability Density Functions for Centerline Velocity Measurements Observed Downstream from the 4.78-mm L/d = 15 Fuel Tube. The distributions were measured at Z = (g) 12 cm; (h) 16 cm; (i) 20 cm. Note that the vertical scale is logarithmic.

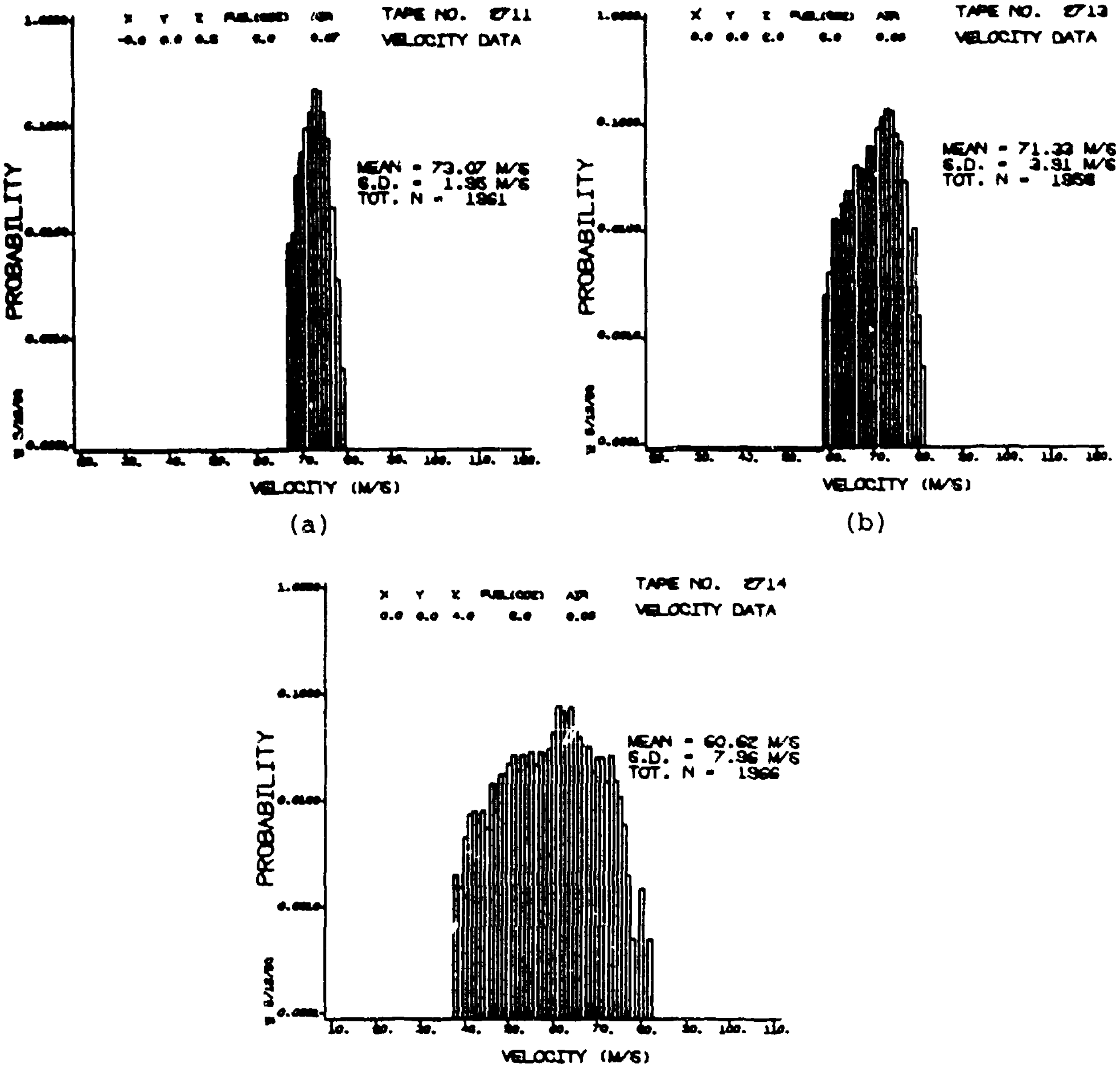

(a) (b)

(c)

Figure 16. Probability Density Functions for Centerline Velocity Measurements Observed Downstream from the 4.50-mm L/d = 80 Fuel Tube. The distributions were measured at Z = (a) 0.5 cm; (b) 2 cm; (c) 4 cm. Note that the vertical scale is logarithmic.

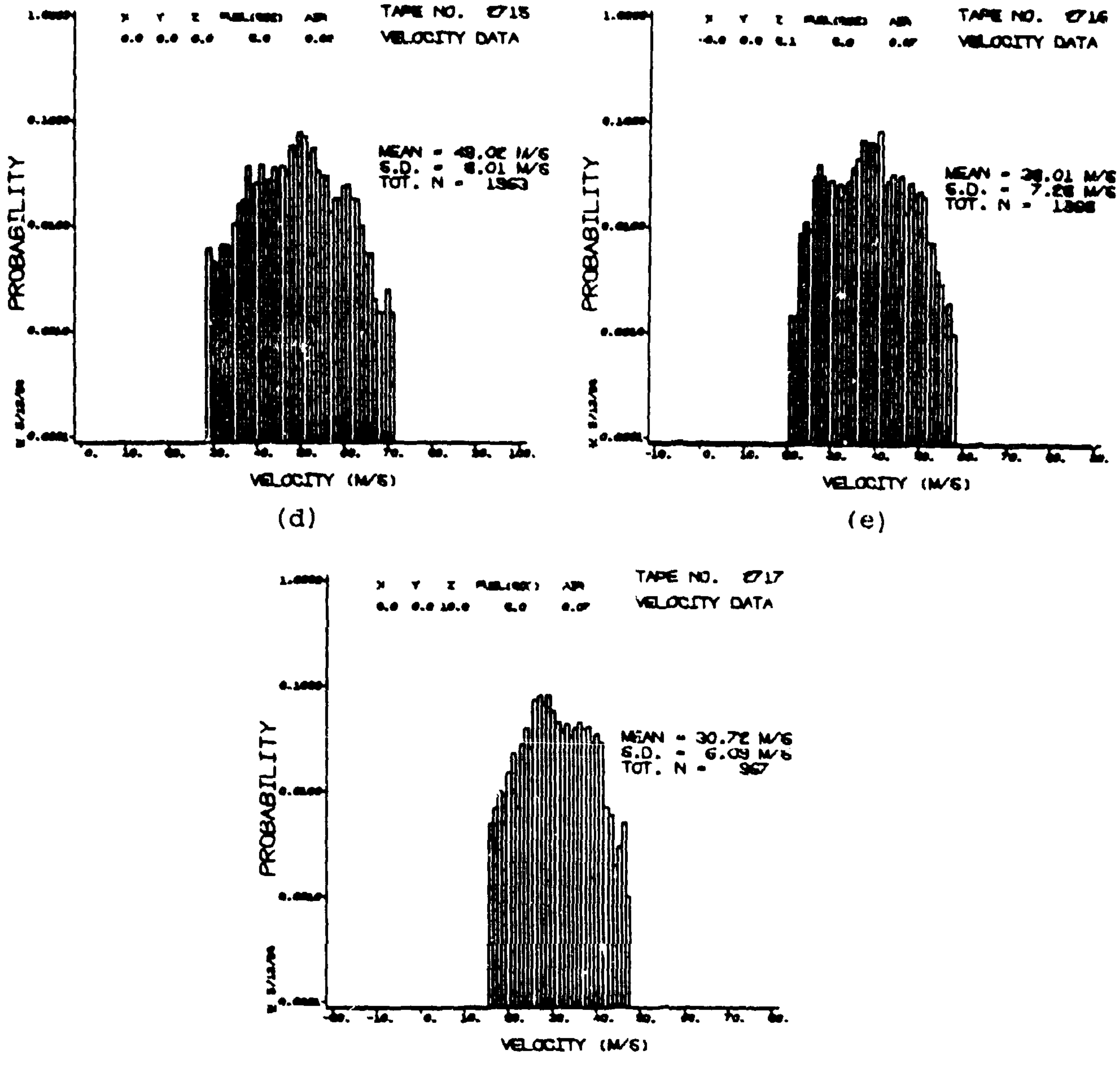

(d)

(e)

(f)

Figure 16. (continued) Probability Density Functions for Centerline Velocity Measurements Observed Downstream from the 4.50-mm L/d = 80 Fuel Tube. The distributions were measured at Z = (d) 6 cm; (e) 8 cm; (f) 10 cm. Note that the vertical scale is logarithmic.

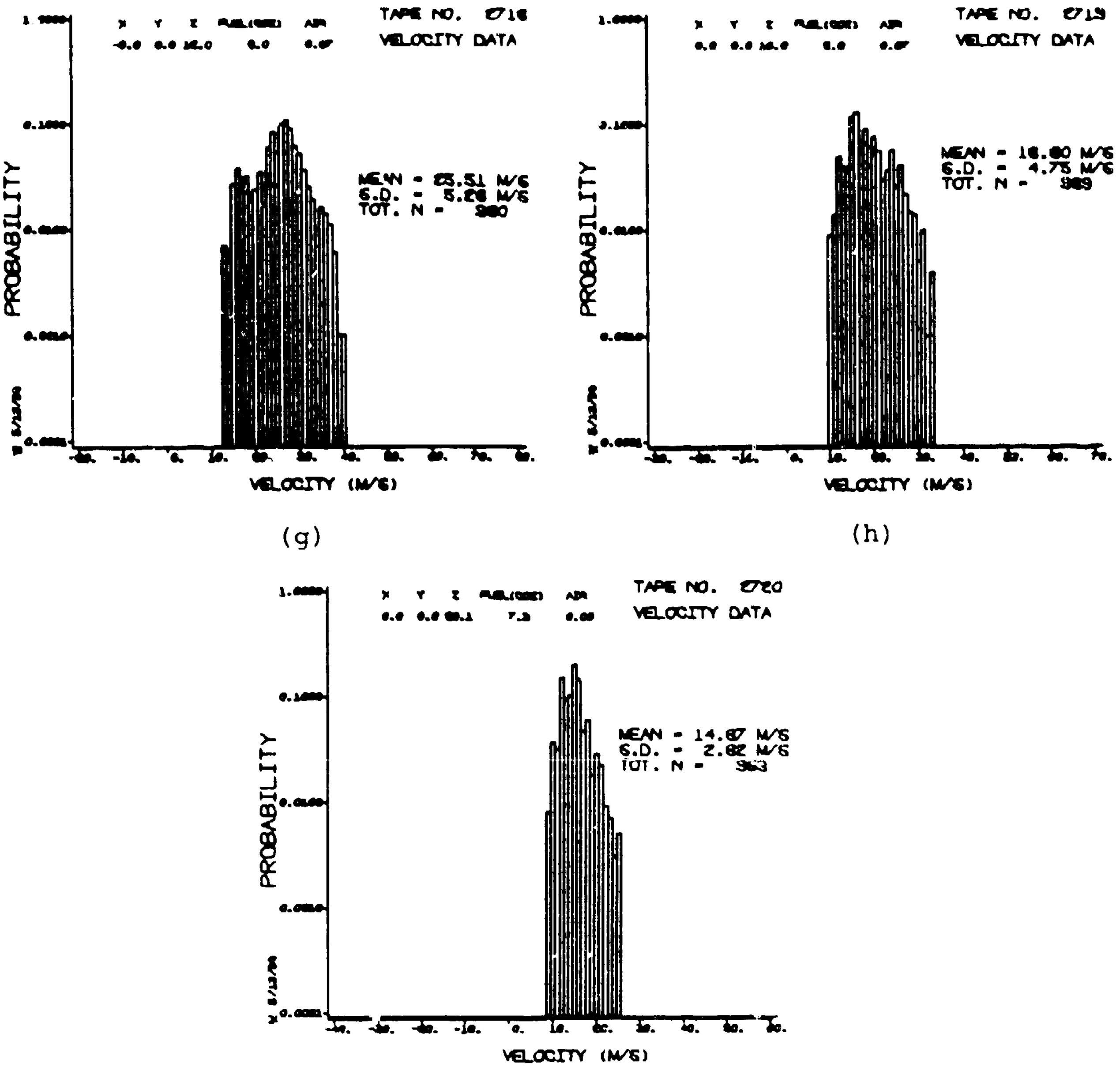

(g)

(h)

(i)

Figure 16. (continued) Probability Density Functions for Centerline Velocity Measurements Observed Downstream from the 4.50-mm L/d = 80 Fuel Tube. The distributions were measured at Z = (g) 12 cm; (h) 16 cm; (i) 20 cm. Note that the vertical scale is logarithmic.

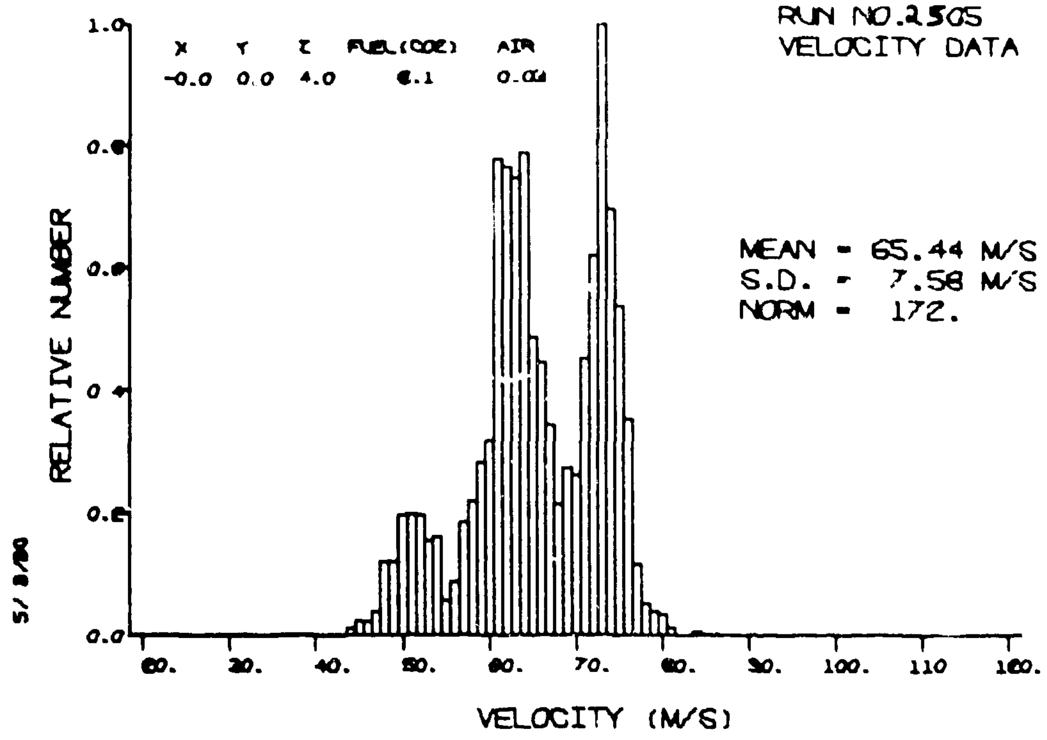

Figure 17. Linear Plot of Figure 15(c) Showing the Observed Velocity 'Modes' in the 'Regular' Fuel Tube Velocity Distributions. This should be compared with the velocity distribution from the 4.50-mm tube (Figure 18).

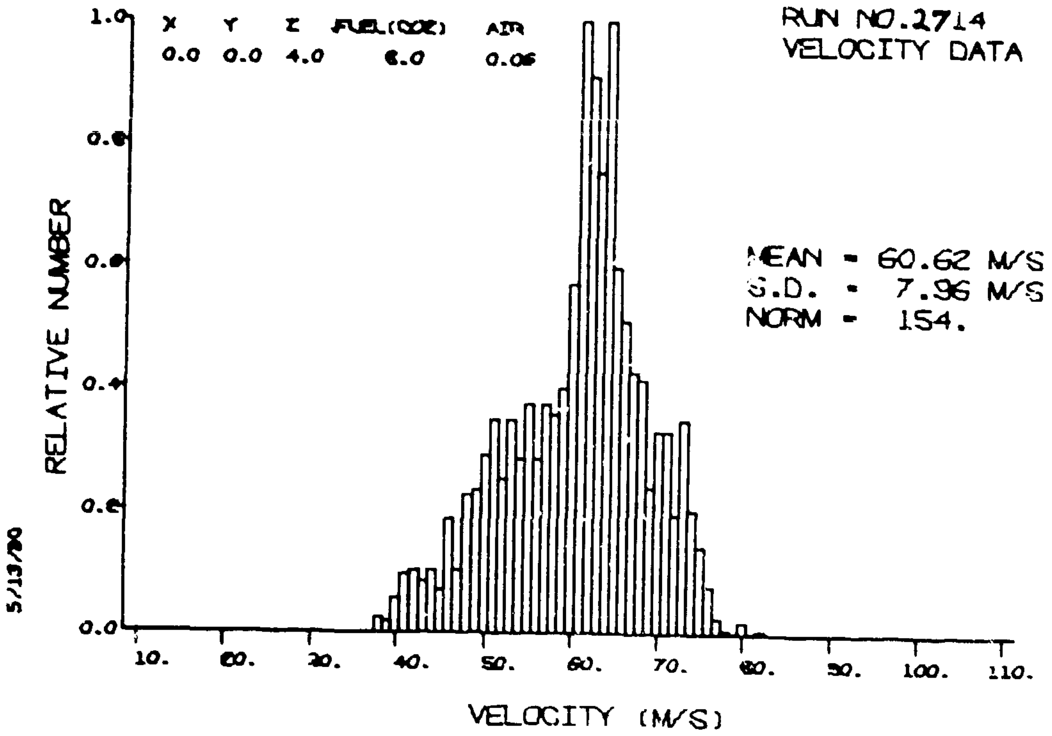

Figure 18. Linear Plot of Figure 16(c) for Comparison with Figure 17.

SECTION V

ISOTHERMAL AND COMBUSTING FLOW MEASUREMENTS

Sections V and VI have been adapted, in part, from the paper by A. J. Lightman, et al., "Velocity Measurements in a Bluff-Body Diffusion Flame," AIAA-80-1544, July 1980.

5.1 MEAN VELOCITIES

The results of two types of experiments are described in this section. In the first type the annular air flow rate is fixed and the fuel flow conditions are varied, while in the second type the fuel flow rate is fixed and the air flow rate is varied. Both types of experiments involve isothermal and combusting conditions with measurements confined to the near-wake region of the bluff body. CO_2 is used in isothermal flow to provide a fuel with the same molecular weight as C_3H_8 used in combusting flows.

The mean axial velocities were measured along the centerline for various flow rates through the central fuel jet. The air flow rate through the annulus was fixed at 2 kg/s. This corresponds to an average annular velocity of 47 m/s and a Reynolds number (Re) of 5.4×10^6 based on the duct diameter of 25.4 cm. For the isothermal experiments, either CO_2 or air was ejected from the fuel jet. Centerline velocity profiles were measured for fuel flows within the limits given in Table 2. Velocity profiles, normalized to the average annulus velocity (W_A), are shown in Figure 19 for five different CO_2 flow rates. The shapes of the velocity profiles obtained with air in the central fuel jet are similar to those given in Figure 19 and are not presented. However, the stagnation points obtained from these data will be discussed later in this section. Figure 20 shows axial velocity profiles made 1 cm off-centerline for CO_2 fuel injection.

TABLE 2
CENTRAL FUEL JET TEST CONDITIONS USING
AIR, CARBON DIOXIDE, AND PROPANE

Fuel	Condition	Fuel Flow Rate (kg/hr)	Est. Exit Temp. (K)	Avg. Fuel Exit Velocity (m/s)	Re ($\times 10^{-4}$)
Air	Min	2	294	27	0.9
Air	Max	9	294	117	4.1
CO_2	Min	4	294	35	2.3
CO_2	Max	16	294	135	8.9
C_3H_8	Min	4	445	53	3.0
C_3H_8	Max	12	400	140	8.6

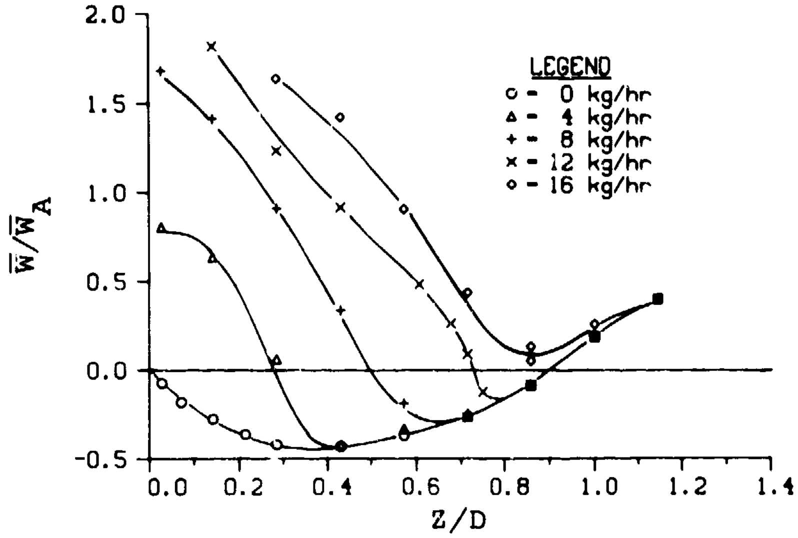

Figure 19. Centerline Profiles of Mean Axial Velocities ($\overline{W}$) for a Fixed Annulus Air Flow Rate of 2 kg/s and Various CO_2 Fuel Flow Rates where $\overline{W}_A$ is the Average Velocity of Annular Flow and Z/D is the Axial Location Normalized to the Centerbody Diameter.

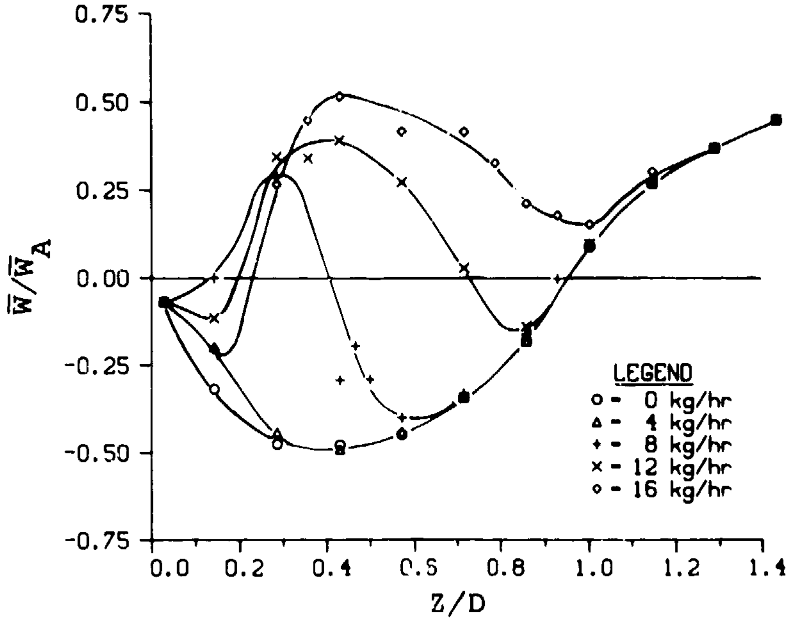

Figure 20. Off-Centerline (1 cm) Profiles of Mean Axial Velocities ($\overline{W}$) for a Fixed Annulus Air Flow Rate of 2 kg/s and various CO_2 Fuel Flow Rates.

The centerline velocity profiles shown in Figure 21 are for combusting flows. The largest uncertainties in the mean velocity measurements occur for these conditions. Durao and Whitelaw[10] also found this to be the case with LDA measurements in the near-wake region of an annular jet. Most of the data points in Figure 21 represent average values of two to six sets of measurements made at different times. Error bars representing plus and minus one standard deviation are shown on several of the data points to indicate the precision of the data in different regions of the flame. It is evident that the errors are largest near the fuel stagnation point.

Figure 22 shows the centerline locations of fuel and air stagnation points for the range of annulus air flow rates given in Table 3. The fuel flow rate was fixed at 4 kg/hr. CO_2 was used for the isothermal experiments and C_3H_8 for the combusting experiments. The locations of the stagnation points were determined from velocity profiles similar to those in Figures 19 and 21 except that the profiles were confined to regions near the stagnation points.

TABLE 3
AIR FLOW TEST CONDITIONS

Condition	Air Mass Flow Rate (kg/s)	Annulus Velocity $\overline{W}_A$ (m/s)	Ref. Velocity In 25.4 cm Duct (m/s)	Re In 25.4 cm Duct ($X\ 10^{-5}$)
Min	0.50	11	8	1.4
Max	2.00	47	33	5.4

The velocity profiles presented in Figures 19 through 21 and the location of the stagnation points cannot be directly compared with previous results, since no previous results appear in the literature for the centerbody configuration. However, the profile for zero fuel flow can be compared with similar data obtained for an annular jet. Durao and Whitelaw[11] used an LDA instrument to measure centerline profiles of mean axial velocities for various air flow rates and various disk diameters. The jet, with an outer diameter of 20 mm, was ejected into still room air. Since the size and design of Durao and Whitelaw's annular jet is very different from that used in this study and since the flow rates are also very different, a direct comparison of results cannot be made. However, the general shape of the zero fuel profile in Figure 19 is similar to their profiles. This is best illustrated by considering their profile for a 14.2-mm diameter disk with a 39.5-m/s air

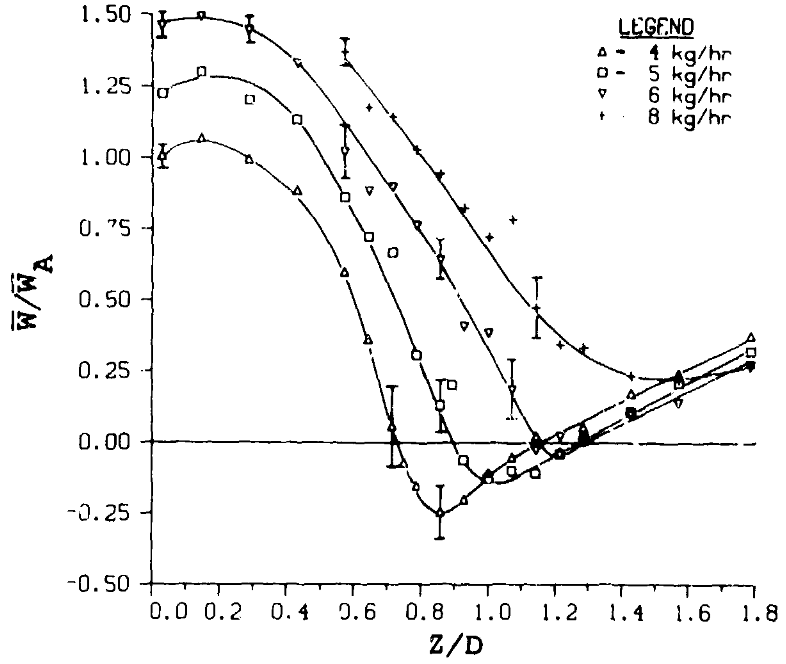

Figure 21. Centerline Profiles of Mean Axial Velocities for Combusting Flows with a Fixed Annulus Air Flow Rate of 2 kg/s and Various Fuel Flow Rates.

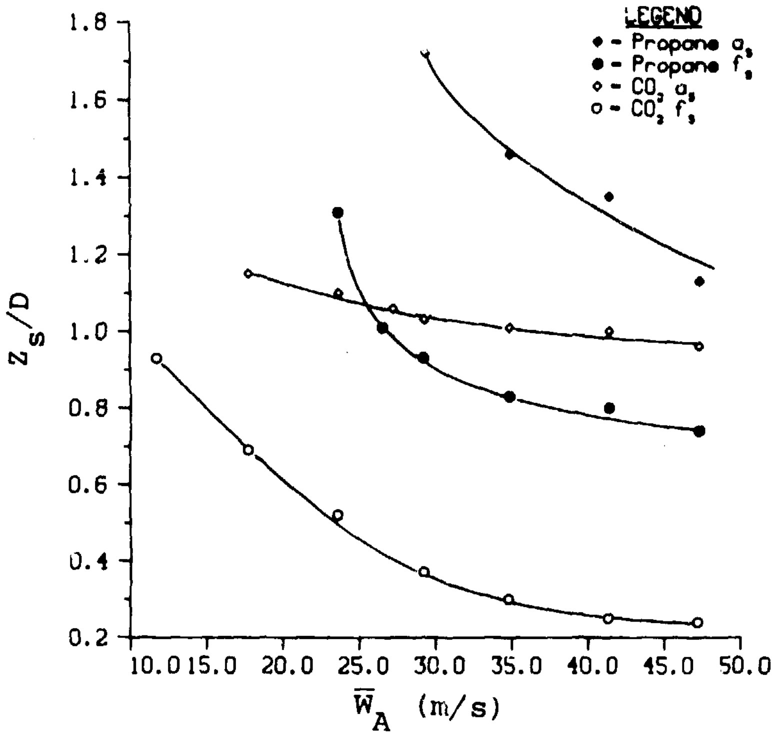

Figure 22. The Variation of the Centerline Location (Z_s) of the Fuel (f_s) and Air (a_s) Stagnation Points with the Mean Annulus Air Velocity ($\overline{W}_A$) for a Fixed Fuel Flow Rate of 4 kg/hr and for Isothermal and Combusting Flows.

flow rate. In this case, their profile shows a peak negative velocity of $\overline{W}/\overline{W}_A = -0.42$ at $Z/D = 0.5$ and a stagnation point at $Z/D = 1.0$. This is almost identical to the zero fuel profile shown in Figure 19 where a peak negative velocity of $\overline{W}/\overline{W}_A = -0.42$ occurs at $Z/D = 0.4$ and a stagnation point occurs at $Z/D = 0.9$. They also observed that as the air flow rate increased, the location of the stagnation point moved towards the disk until a location was reached, $Z/D = 1.0$, where an additional increase in flow rate did not change the location of the stagnation point. This trend is illustrated somewhat for the air stagnation points for isothermal flow shown in Figure 22.

The influence of the fuel flow rate on the location of the fuel stagnation point has been examined in detail. The centerline results for isothermal flow for both air and CO_2 and for combusting flow are shown in Figure 23. Because of the early penetration of the fuel jet along the centerline, only three data points are available under combusting conditions for the 2 kg/s air flow rate. The data exhibit a linear behavior for the centerline fuel stagnation point distance with the initial centerline fuel velocity. As expected, the slope of the straight line for combusting flow is less than that for cold flow. Although not shown in the figure, the off-axis data for CO_2 also reveal a linear dependence of the fuel stagnation point distance with the initial fuel velocity and with a slope about the same as that for the centerline data. The observations of the linear behavior of the fuel stagnation point are somewhat surprising since the near-wake region is characterized by a strong recirculation zone. To gain insight into the flow conditions in the vicinity of penetration (both for position and mass flux conditions) some radial profiles were measured. Figure 24 show profiles taken slightly upstream of the fuel stagnation position so that the zero fuel flow condition will show the recirculation zone. As the fuel flow is increased the jet becomes evident and eventually penetration occurs along the centerline.

In another set of data in which the annular flow was varied, the fuel flow necessary to maintain the fuel stagnation point at a fixed location ($Z/D = 0.4$) was determined. Again there appears to be a linear dependence between this set of variables (Figure 25).

5.2 TURBULENCE INTENSITIES

The centerline turbulence intensity profiles in Figure 26 are associated with the mean axial velocity profiles in Figure 19. A comparison of the zero fuel flow profiles in these two figures shows that the peak turbulence intensity occurs very near the air stagnation point. Similar results are noted for the off-axis zero fuel flow profiles in

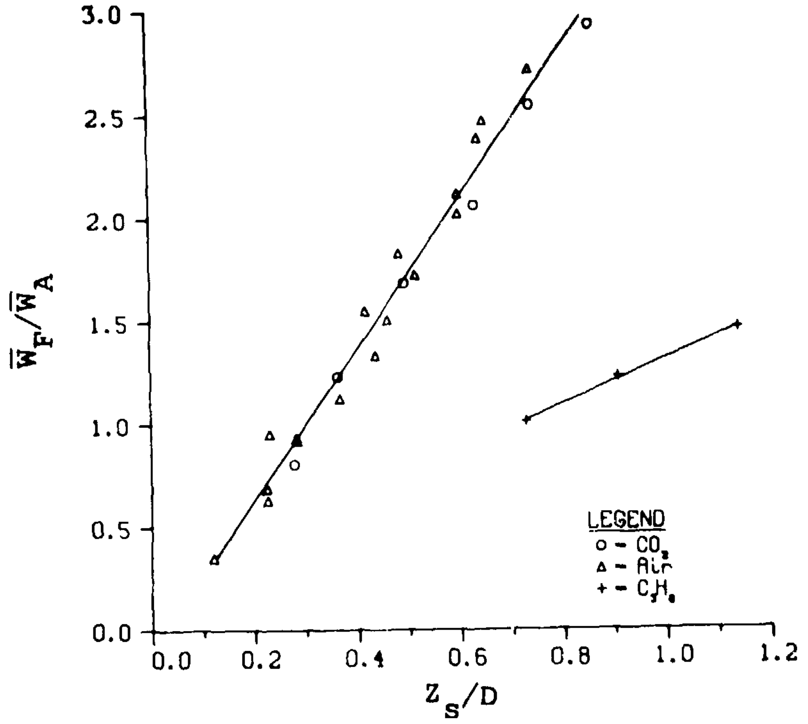

Figure 23. The Relationship between the Centerline Fuel Exit Velocity ($\overline{W}_F$) and the Centerline Location of Fuel Stagnation Point (Z_s/D) for Isothermal and Combusting Flows.

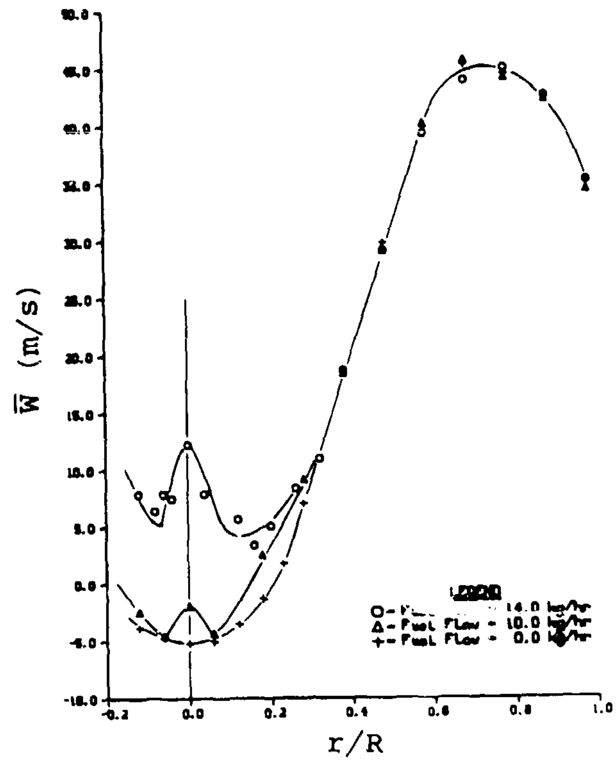

Figure 24. Radial Scan of Axial Velocity Measured at $Z = 12$ cm, Upstream of the Air Stagnation Position, Showing the Effect of Fuel Flow. The two non-zero fuel flows shown correspond to pre- and post-penetration conditions.

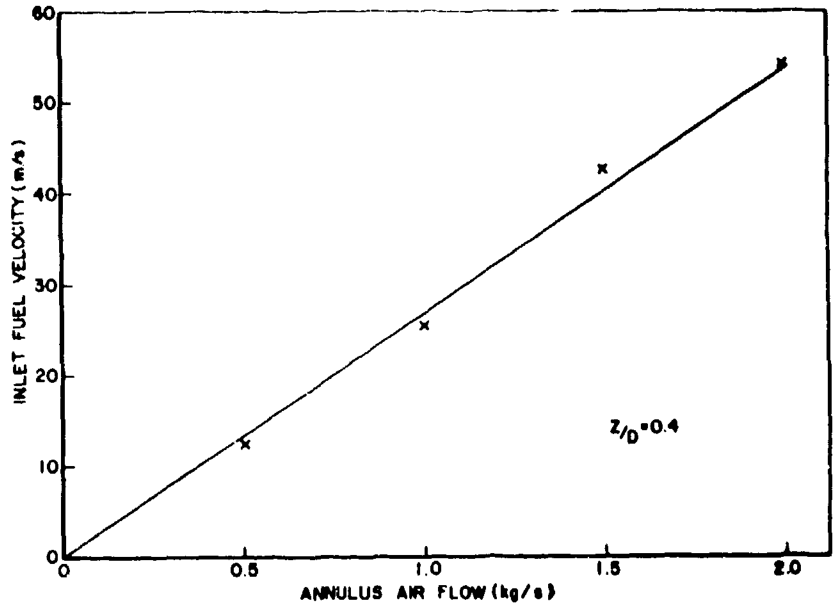

Figure 25. Fuel Flow (Velocity) Required to Maintain the Fuel Stagnation Point at Z/D = 0.4 when Varying the Annulus Flow.

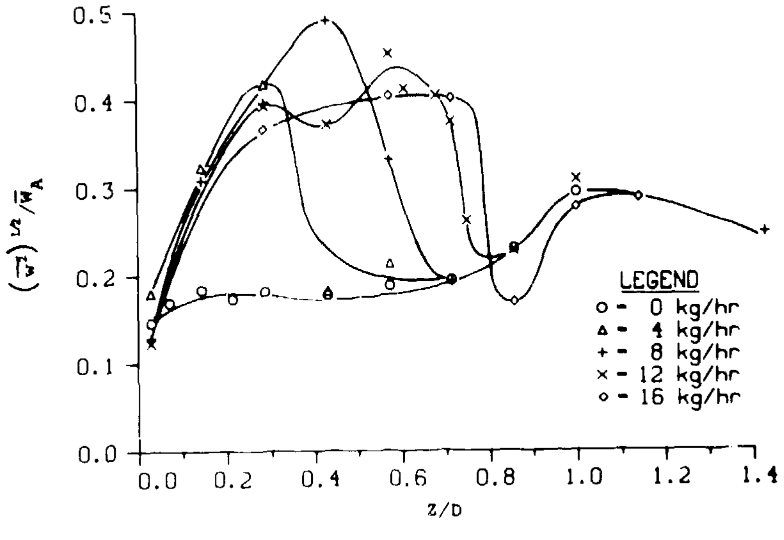

Figure 26. Centerline Profiles of the Axial Component of Turbulence Intensity for a Fixed Annular Air Flow Rate of 2 kg/s and Various CO_2 Fuel Flow Rates.

Figures 20 and 27. In addition, these off-axis profiles show that the minimum turbulence intensity occurs at the same Z/D location as the peak negative velocity. These results are somewhat different than those obtained by Durao and Whitelaw[11] for the annular jet. Their centerline profiles show a gradual decline in turbulence intensity as Z/D increases; however, there are two peaks corresponding approximately to Z/D locations of the maximum negative velocity and the air stagnation point. The magnitude of the turbulence intensities for their jet and those presented here agree within about 7 percent.

The maximum turbulence intensity for the axial component of the velocity occurs near the fuel stagnation point for both isothermal and combusting flows. This is noted for isothermal flows by examining the centerline profiles in Figures 19 and 26 for a CO_2 flow rate of 12 kg/hr. The turbulence intensity peaks at a $Z/D = 0.65$ and the fuel stagnation point occurs at $Z/D = 0.7$. Just downstream of the fuel stagnation point the turbulence intensity decreases rapidly and then becomes essentially the same as that for a zero fuel flow. This description also applies to the off-axis profiles shown in Figures 20 and 27 except for the flow rates of 4 and 16 kg/hr that do not have fuel stagnation points. A comparison of the centerline profiles for combusting flows in Figures 21 and 28 also shows a similar result even to the point where the turbulence intensities downstream of the fuel stagnation points have about the same magnitude as the isothermal zero fuel flow profile shown in Figure 26.

5.3 VELOCITY PDF'S NEAR STAGNATION LOCATIONS

The phenomena of well-defined velocity "modes" were noticed in the centerline flowfield measurements, similar to the free jet observations. In the case where the annulus is also flowing, similar "mode" structures become evident in the vicinity of the air stagnation point. They are present for all the fuel tubes, indicating that they result from the fluid dynamic interaction of the entire system and not from the inlet flowfield alone, as indicated for the free jet observations. Examples of the pdf's are shown in Figure 29, plotted linearly. When examined in detail, the "modes" appear to be at fixed velocities, the same velocities for each measurement location. But the relative probabilities change, yielding the smooth variation in average velocity reported. The velocities at which the "modes" occur are dependent upon the operating conditions of the combustor.

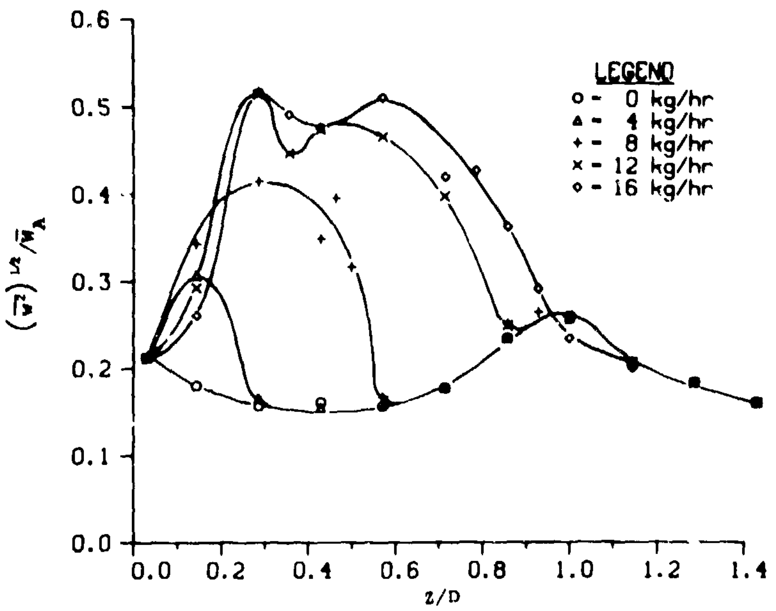

Figure 27. Off-Centerline Profiles of the Axial Component of Turbulence Intensity for Various CO_2 Fuel Flows with a Fixed Annular Air Flow Rate of 2 kg/s.

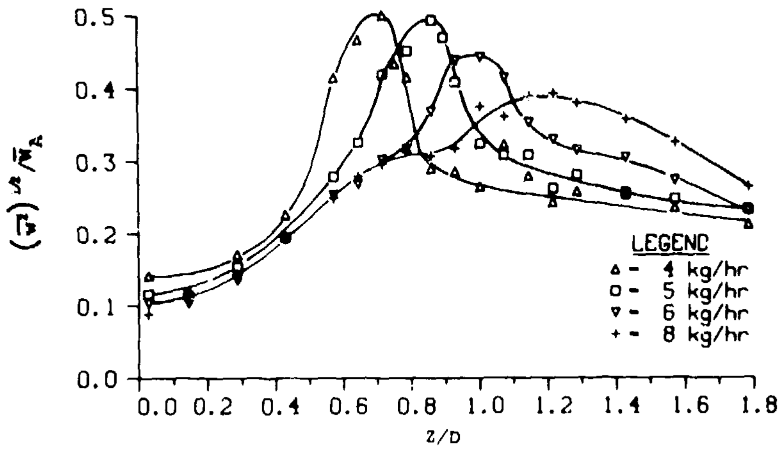

Figure 28. Centerline Profiles of the Axial Component of Turbulence Intensity for Combusting Flows with a Fixed Annulus Air Flow Rate of 2 kg/s and Various Fuel Flow Rates.

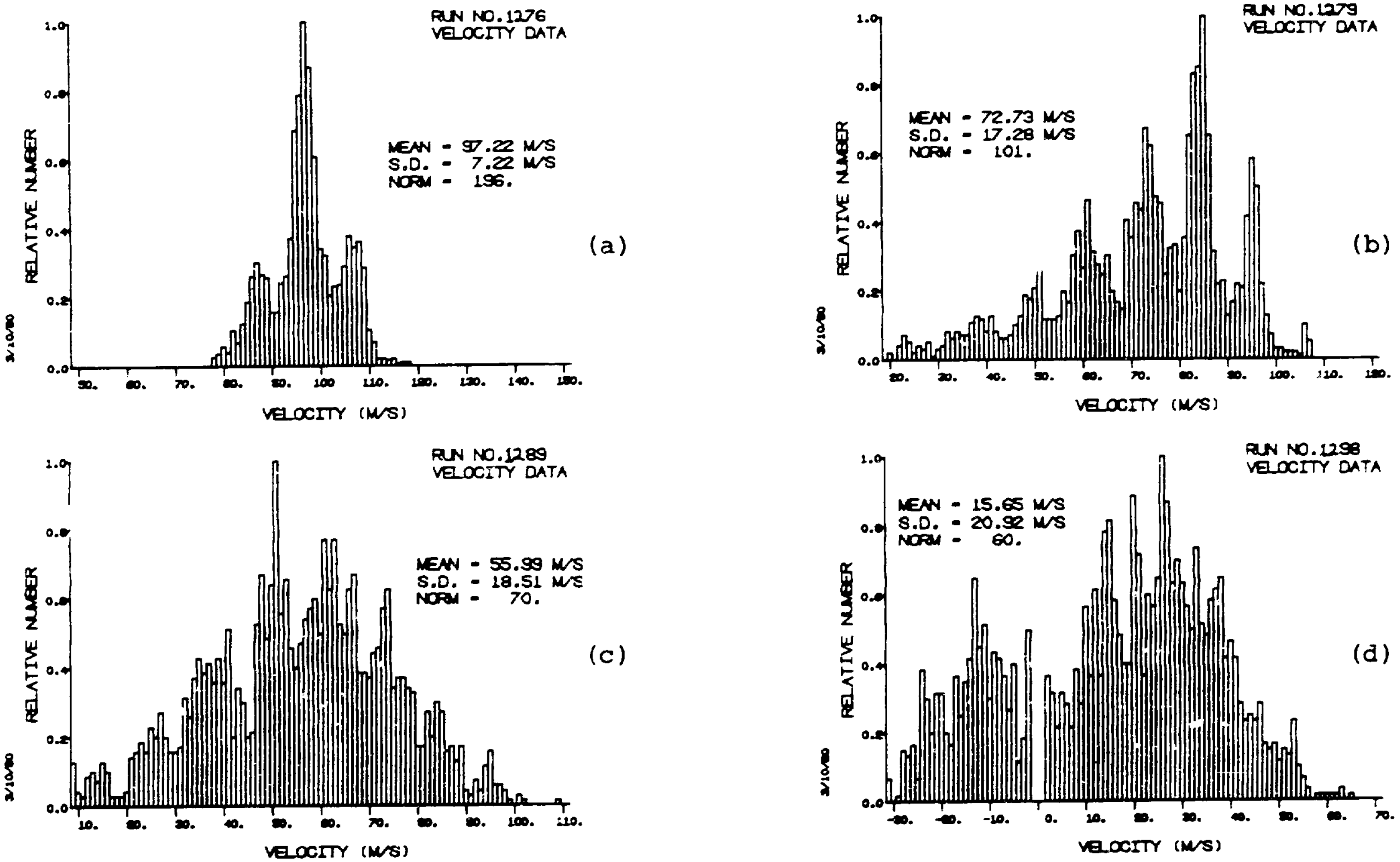

Figure 29. Examples of the "Modal" Axial-Velocity Distributions Observed at Locations through the Fuel and Air Stagnation Positions. Measurements were taken at Z = (a) 0.4 cm; (b) 2 cm; (c) 4 cm; (d) 8 cm respectively on centerline with a fuel flow of 10 kg/hr CO_2 and an annular flow of 2 kg/s.

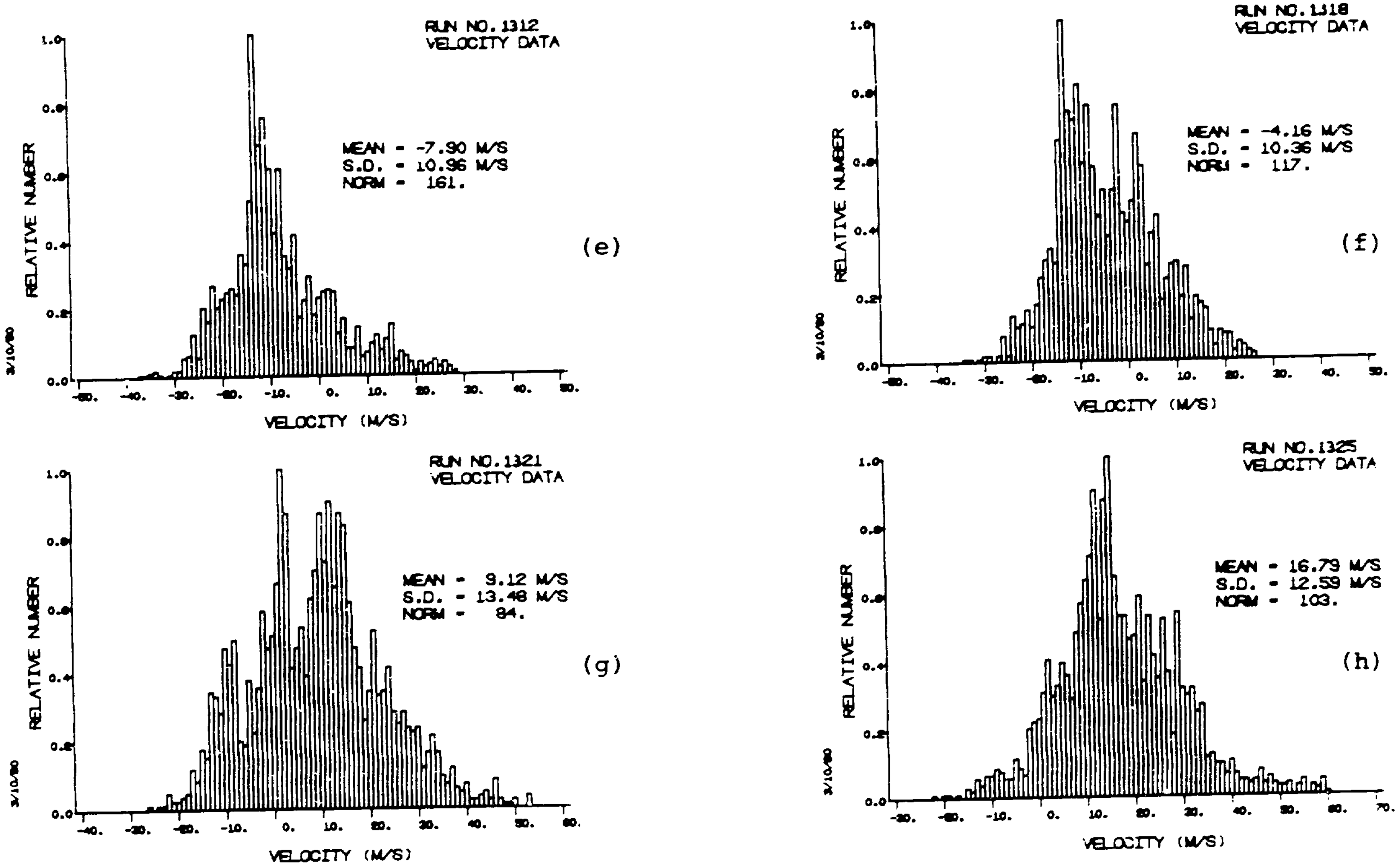

Figure 29. (continued) Examples of the 'Modal' Axial-Velocity Distributions Observed at Locations through the Fuel and Air Stagnation Positions. Measurements were taken at Z = (e) 10 cm; (f) 12 cm; (g) 14 cm; (h) 16 cm respectively on centerline with a fuel flow of 10 kg/hr CO_2 and an annular flow of 2 kg/s.

SECTION VI

FLOWFIELD IMPLICATIONS

The discussion in this section is concerned with the velocity profile data in the near-wake region of the bluff body, their implications on the flowfield, and combustion characteristics within the framework of certain predicted flowfields.[12] The combustion tunnel can be viewed as dual coaxial jets with the annular air comprising one jet and the fuel injected from the central tube being the other jet. The isothermal flow observed is delineated by five regimes of operation in the following discussion. The combusting flow observations are explained with reference to the flowfields that are based upon recent isothermal predictions. An interesting feature of this configuration is the dramatic change in flame structure that occurs as the fuel to air ratios are varied, as reported by Roquemore, et al.[13] The illustrative figure in each paragraph is qualitatively based upon the predicted flow pattern in the top half of a cross section of the axisymmetric flowfield. The solid lines represent typical flow paths encountered.

6.1 NO ANNULAR FLOW

The flow issuing from the fuel tube has the character of a simple jet. The duct radius is larger than the typical fuel tube radius by a factor exceeding 50 and can be considered as infinitely distant, at least for the first 50 fuel-tube diameters downstream. The flow is shown in Figure 30. A weak recirculation vortex will be set up by the fuel flow, due to the duct boundary, but it is of no practical significance in the region of the measurements.

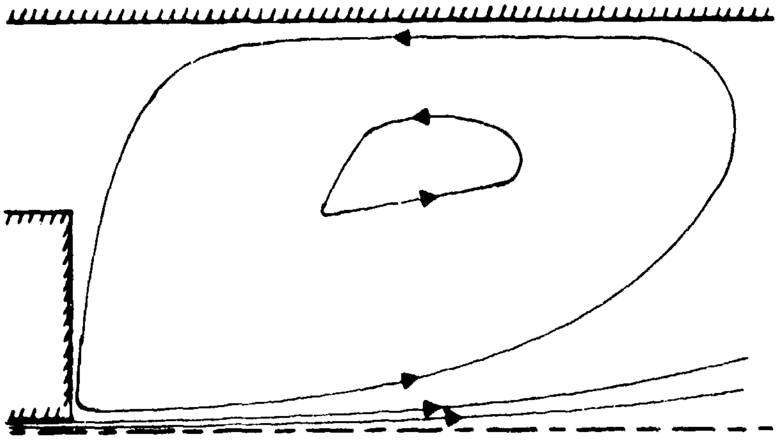

Figure 30. Flowfield for Fuel Flow in the Combustion Tunnel with No Annular Flow.

The observations of this type of flow were presented in Section IV and compared with results obtained for true free jets. In the region of observation the experiments agree with those in the literature.

6.2 NO FUEL FLOW

The annular flow enters the combustor around the centerbody. A wake will be present behind the centerbody, extending downstream a length on the order of the centerbody diameter. Within the wake a toroidal recirculation zone is set up, creating a reverse jet on the centerline, issuing upstream (Figure 31). This reverse flow will be in direct opposition to a central jet when one is present. Hence other regimes of operation will depend upon the relative strengths of the annular and central jets.

Centerline and off-centerline measurements of the axial velocity were made for zero fuel flow and 2 kg/s annular air flow, Figures 19 and 20. The upstream flowing jet starts at about 0.9D from the centerbody face and reaches a maximum axial velocity of about half the entrance velocity near 0.4D.

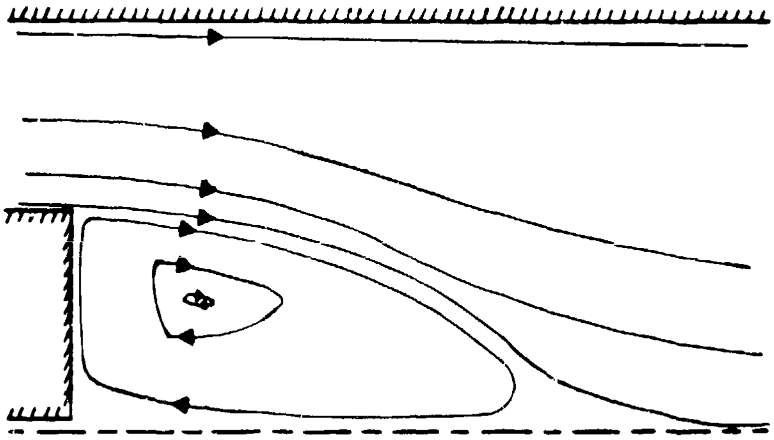

Figure 31. Flowfield for Annular Flow in the Combustion Tunnel with No Fuel Flow.

6.3 FUEL JET MUCH WEAKER THAN ANNULAR REVERSE-FLOW JET

In this situation the reverse jet created by the annular flow is so strong that it stops the fuel jet as it enters, reversing it so that it flows back along the face of the centerbody. The fuel is then entrained in the annular flow and carried downstream (Figure 32). The recirculation region resulting from the annular flow will be pushed away from the fuel entrance, allowing the fuel to enter the flowfield.

The centerline axial velocities for this flow condition are characterized by a positive issuing velocity from the fuel tube which decays to zero in a short distance downstream. The reverse annular air jet becomes the dominant flow determining the velocity field. The axial velocity measurements then become the same as those measured for the case of no fuel flow (Paragraph 6.2) This type of flow pattern is demonstrated in Figure 19 for a fuel flow of 4 kg/hr. A lesser fuel flow would illustrate the expected flowfield even better.

The fuel is entrained in the annular flow at the face of the centerbody and then flows downstream. In combusting flow the observed flame is cylindrical in shape extending from the edges of the centerbody, visually demonstrating this flow condition.

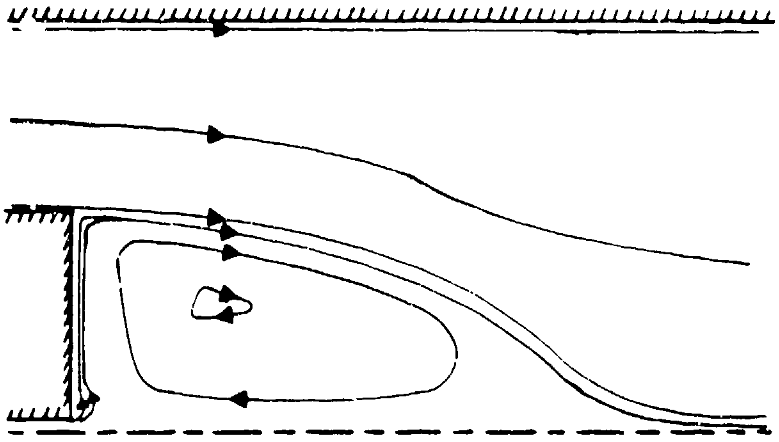

Figure 32. Flowfield in the Combustion Tunnel when the Fuel Jet is Much Weaker than the Reverse Jet Arising from the Annular Air Recirculation.

6.4 FUEL JET SLIGHTLY WEAKER THAN ANNULAR REVERSE-FLOW JET

This flowfield (Figure 33) is characterized by two positions where the centerline axial velocities are zero. The upstream stagnation position is the location at which the annular jet overcomes the fuel jet and reverses the fuel flow. The second stagnation point, further downstream, is that of the annular air jet discussed previously. With a fixed annular flow, the fuel stagnation position moves downstream as the strength of the fuel jet increases (Figure 23). However, the location of the second stagnation point does not appear to be affected by the fuel flow rate. The motion of the fuel stagnation position downstream appears to depend linearly upon the fuel inlet velocity (Figure 23). Numerical computations[14] for the flowfield with these operating conditions predict nonlinear behavior, but the nonlinearity is not pronounced over the extent of the experimental operating conditions.

When the fuel flow is kept constant, the fuel stagnation position moves upstream as the annular jet increases in strength (Figure 22). The air stagnation location also moves upstream as the annular air flow rate is increased (Figure 22), the shift being greater for combusting conditions than for isothermal flow. To maintain the fuel stagnation position at a fixed location, the fuel flow and annular air flow must be varied in the same manner (Figure 25), with an apparently linear relationship.

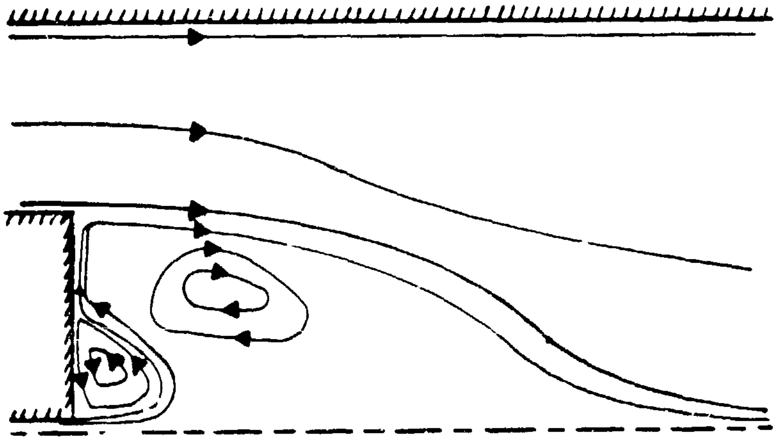

Figure 33. Flowfield when the Fuel Jet is Slightly Weaker than the Annular Air Recirculation Jet. Note the counterrotating recirculation vortices.

The flow path of the fuel creates another recirculating vortex near the centerbody face, rotating in direction opposite to the vortex created by the annular air flow. The off-centerline axial velocity profiles (Figure 20) show a third stagnation position between $Z/D = 0.1$ and 0.2 for CO_2 flows greater than 4 kg/hr. These stagnation points indicate the presence of a fuel recirculation zone near the jet exit. The intensity and size of the recirculation zone increase with increasing CO_2 flow rate as indicated by the increase in peak negative velocity and the downstream movement of the stagnation points with increasing CO_2 flow rate. The noted increase in size of the recirculation zone also implies that the angle of spread of the fuel jet decreases with increasing CO_2 flow rate.

As expected, there are some differences between the velocity profiles for isothermal and combusting flows. The centerline profiles for combusting flows (Figure 21) show a significant potential core region near the fuel jet exit that is not as evident for the cold flow profiles in Figure 19. This is consistent with recent observations by Yule and Chigier[15] that combustion causes a significant increase in the length of the potential core of a ducted jet. It is also apparent in comparing Figures 19 and 21 that combustion results in a downstream shift in the locations of both the fuel and air stagnation points. This is not consistent with the results of Durao and Whitelaw[11] who observed that the air stagnation point for a 20-mm diameter jet with a 14.2-mm diameter disk is not affected by combustion. This difference might be due in part to the influence of the fuel jet on the location of the air stagnation point that can be observed in Figure 21.

In combusting flow the observed flame structure is that of the cylinder described in Paragraph 6.3 with the addition of a flame ball sitting on the centerline about the position of the fuel stagnation location. The existence of this flame ball demonstrates the intense mixing of the fuel and air jets in the vicinity of the fuel stagnation position. The fact that the turbulence intensities increase rapidly and peak near the fuel stagnation position (Figure 28) demonstrates the existence of this intense mixing. Remaining unburnt fuel is entrained in the annular flow and burns in the cylindrical flame described above.

6.5 FUEL JET MUCH STRONGER THAN ANNULAR REVERSE-FLOW JET

When the fuel jet has sufficient strength to overcome the annular reverse-flow jet, it penetrates the recirculation region and pushes it off the centerline. In this situation (Figure 34), the fuel issues as a conical jet downstream. The annular flow is drawn down near the face of the centerbody and entrained in the fuel flow directly. A recirculation vortex is set up against the face of the centerbody adjacent to the annulus, the size of the vortex depending on the relative strength of the two jets. At sufficiently high fuel flow, numerical calculations predict[12] that the vortex will disappear.

The centerline axial velocity measurements (Figure 19) show that with CO_2 as the fuel, the fuel jet penetrates at a flow of 16 kg/hr. For the combusting flow the penetration occurs at a lower fuel flow of 8 kg/hr (Figure 21), affected by the energy released in combustion. The resulting flame front becomes conical as expected for this flow condition. A cylindrical flame is still observed because the annular jet is so strong that some fuel is entrained into the annular jet shear layer.

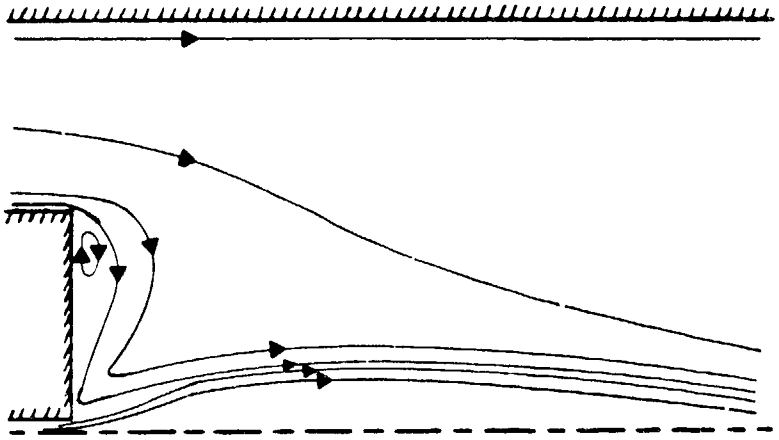

Figure 34. Flowfield when the Fuel Jet is Much Stronger than the Air Recirculation Jet. As the fuel jet strength increases the recirculation region on the centerline disappears.

SECTION VII

CONCLUSIONS

Measurements have been made of the axial velocity in an axisymmetric flowfield characterized by an annular jet input around a centerbody, and a fuel jet input on the centerline. The measurements have been taken using a variety of fuel tubes, fuels, and relative flows of fuel and annulus air, and in isothermal and combusting flows.

When the annulus air is turned off or reduced to a practical minimum, the fuel tube velocity profiles show the behavior of the traditional free jet. This is to be expected in view of the small size of the fuel tube relative to the duct. The turbulence intensity variation as a function of axial location also behaves as for a free jet. Interest has been taken in the shapes of the velocity distributions (pdf's) at the various axial locations. The distributions show velocity 'modes' (preferred velocities) whose existence appears to depend upon how the inlet flow is prepared.

Measurements were made with both annular air and fuel flowing, at room temperature and in combustion. Most of the features of the flowfields established by measurements in isothermal flows are also present in combusting flows with the primary difference being in magnitude. For a fixed annular air flow rate, the centerline location of the fuel stagnation point appears to increase linearly with an increase in the centerline fuel exit velocity. The location of the air stagnation point depends primarily on the flow rate of the annular jet which agrees with the findings of Durao and Whitelaw.[11] The location of the centerline air stagnation point does not appear to be altered by the fuel flow rate so long as the fuel flow rate is below that required for penetration of the recirculation region.

Penetration along the centerline occurs at much lower fuel flow rates for combusting flows than for isothermal flows. Penetration on-centerline occurs at a lower fuel flow rate than does penetration off-centerline. The fuel and air stagnation points move downstream for combusting flows as compared to isothermal flows with the location of the fuel stagnation point being moved the most. For a fixed fuel flow rate, the locations of both the fuel and air stagnation points decrease asymptotically to different values as the annulus flow rate is increased. The turbulence intensity appears to peak near the fuel stagnation point and to drop abruptly just downstream of the fuel stagnation point.

When the velocity distributions are examined, it is observed that there are velocity 'modes' in the measurements taken near the air stagnation point. These are thought to arise from the complex interplay of the flowing fluids and the physical structure containing them. A more detailed study will be needed to explain these "modes."

The measured velocity profiles conform to the flowfields expected. These flowfields show large spatial gradients. Therefore, off-centerline velocity profiles should measure at least two components of the velocity field simultaneously. This information, along with Reynolds stress data, will be required in future computer model evaluation for this combustor.

APPENDIX A

SAMPLE SIZE REQUIREMENTS

There has been considerable discussion among scientists measuring distributions of variables, concerning the minimum sample size required to define the moments of the distribution. As the LDA system records individual realizations of velocity for a preselected number of samples, a study was made of the sample size required for the measurements reported here. Clearly, recording the minimum number needed, consistent with the accuracy desired, optimizes the time usage of the instrument. Care must be exercised that the samples are distributed about a stationary mean and that there is no long term variation that will alter the mean value.

A computer study was made to gain understanding of the variations of the moments of the distribution as a function of sample number. A record of 5,000 samples was taken. This was used to populate five records of sizes 200, 500, 1,000, 2,000, and 5,000 samples, and the relevant parameters for each sample distribution were computed. The results are given in Table A.1.

TABLE A.1
DISTRIBUTION PARAMETERS AS A FUNCTION OF SAMPLE SIZE

SAMPLE SIZE	MEAN	STANDARD DEVIATION	SKEWNESS	KURTOSIS
200	29.6	8.02	-0.47	2.65
500	30.6	8.29	-0.16	3.49
1,000	30.9	8.74	-0.19	3.50
2,000	31.0	8.88	-0.23	3.38
5,000	30.7	8.97	-0.27	3.40

The first moment yielding the average velocity stabilizes first, with practically the smallest sample size. The second moment, from which the standard deviation is derived, stabilizes once the sample size is 1,000. As a common practice all data in this study were sampled for 2,000 realizations, provided that the time required was not overly long. The distributions obtained with the 200-sample and the 5,000-sample records are shown in Figure A.1. The main features appear similar but the relative weights are different. The 5,000-sample record is smoother in appearance with the features more easily discernable.

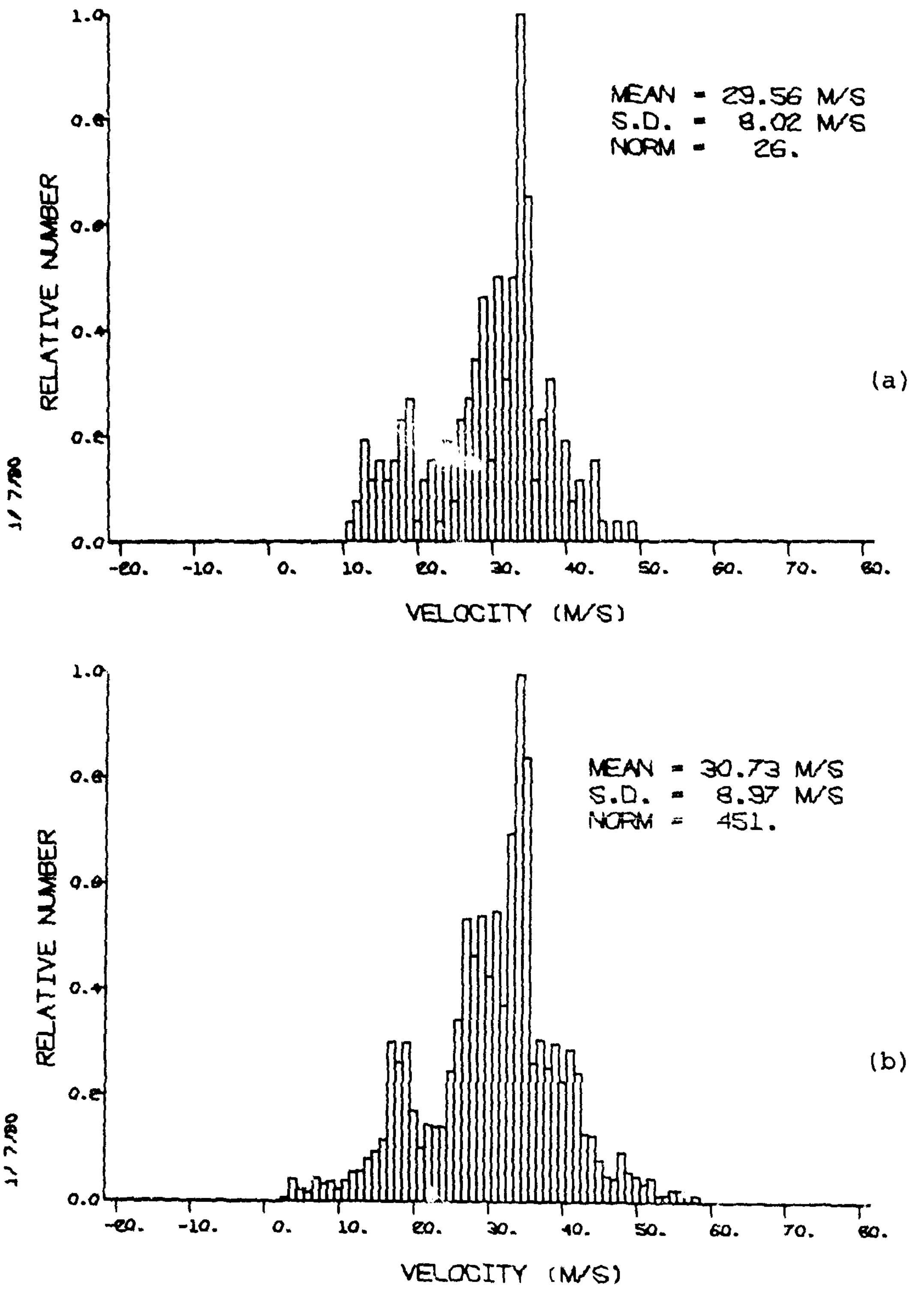

Figure A.1. Probability Density Functions for the Velocity Realizations with Differing Total Numbers (a) N = 200; (b) N = 5,000.

APPENDIX B

LDA SPOT SIZE EFFECT

The LDA apparatus measures realizations of the velocity within its finite spot size, an ellipsoid approximately 150 μm in diameter x 1.5 mm long. The spot size will not produce a simple integration of the velocity over that region of space if the number of seed particles passing through is proportional to the local velocity, as claimed by McLaughlin and Tiederman.[B.1] In this case the measured average velocity V_M, obtained from a time average of all the velocity realizations, is given by

$$V_M = \sum_i n_i v_i / \sum_i n_i \tag{B.1}$$

where n_i, the number of realizations of v_i, is proportional to v_i. Then

$$V_M = \sum_i v_i^2 / \sum_i v_i \tag{B.2}$$

This can be extended to investigate the effect on the flowfield measurements at the fuel tube entrance plane, the spatial region where the effect is most noticeable due to the high spatial gradients in the flowfield.

The problem is reducible to a one-dimensional analysis with little loss in detail since the aspect ratio of the LDA spot is so large (10:1), and since all transverse profiling is along a symmetry plane (i. e., through the origin). Consider an LDA spot centered at R_o, so that the measurement, V_M, will be associated with this location, and extending $\pm\Delta R$ about R_o.

$$V_M = \int_{R_o - \Delta R}^{R_o + \Delta R} v^2(R)\,dR \Bigg/ \int_{R_o - \Delta R}^{R_o + \Delta R} v(R)\,dR \tag{B.3}$$

where v(R) is the analytic velocity at radial position R.

For the "regular" fuel tube, where the exit velocity profile might be that of a transition flow,[B.2]

$$v(R) = v_o(1-2R/d)^{1/7} \qquad (B.4)$$

where d is the fuel tube diameter, and v_o is the peak (centerline) velocity.

The expression for V_M can be integrated analytically. The results for this numerical evaluation for a scan in the X direction, where $\Delta R = 0.75$ mm, and in the Y direction, where $\Delta R = 0.075$ mm, are shown in Figure B.1. The wings resulting from the instrumental broadening are clearly evident, the X direction scan being broadened considerably more than the Y direction scan, as would be expected from their respective ΔR's. The velocity profile given in Equation B.4 is shown in Figure B.1 as the solid curve, for reference. Since the broadening manifests itself at the farthest radial location, the encompassed area can provide a large additional contribution to the fuel tube area measurement, and the resulting false contribution to the mass flux would be substantial. Although the Y scan broadening shown in Figure B.1 does not appear extensive, the contribution to the mass flux is still sufficient to produce a 10 percent error.

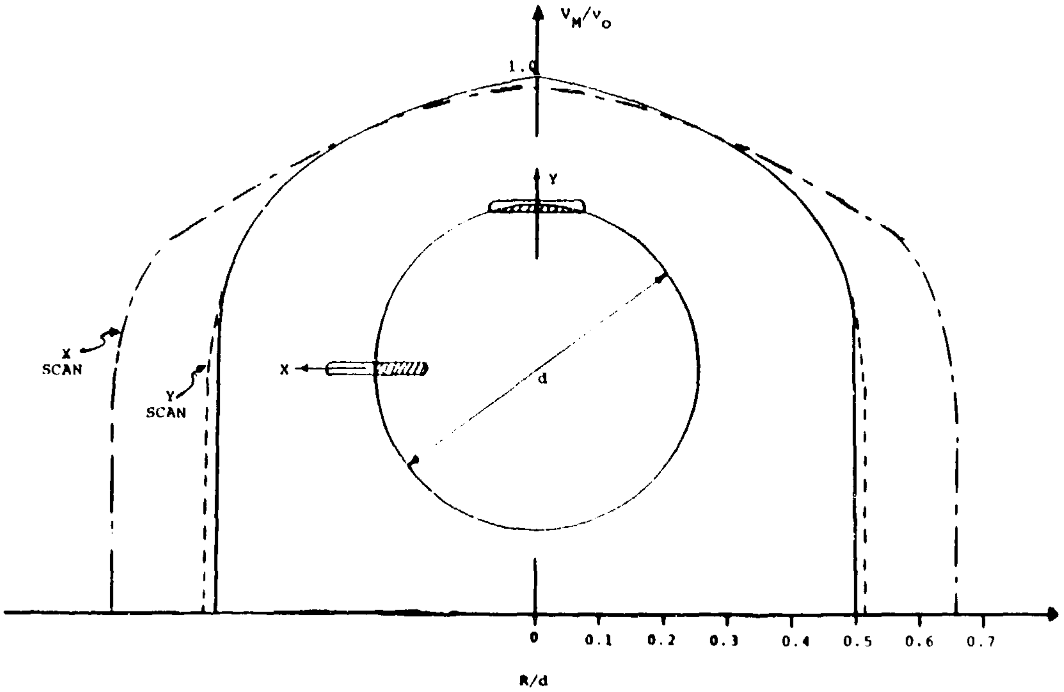

Figure B.1. Effect of Spot Size on the Measurement of Fuel Tube Entrance Profiles. The fuel tube and LDA spots shown are reduced by a factor of two from the rest of the diagram.

APPENDIX C

HIGH VELOCITY DIFFICULTIES

The axial velocity measurements were limited to <120 m/s, for reasons not anticipated. The Doppler burst is composed of a signal (a-c magnitude) and a pedestal, as shown in Figure C.1. When working with forward scattered signals, the pedestal can be very much larger than the signal, especially if agglomerated seed particles enter the measurement volume. A typical signal is shown in Figure C.2. At higher velocities the time width of the pedestal shortens; typically at 120 m/s the pedestal from a scatterer crossing a 120 μm spot diameter will be 1 μs wide. If the pedestal is Gaussian, its frequency content would extend to about 1 MHz.

The problem was that the pedestal was not perfectly Gaussian. As a result there exist frequency components at harmonics of the basic frequency. In the case of large particle scattering, the amplitude of the harmonics can be substantial, so that the signal level of the harmonics that pass through the high-pass filter (used to remove pedestals) can be comparable to an actual Doppler signal amplitude, as shown in Figure C.3. The result is that the processor confuses the real signal and the harmonics and gives erroneous results. The onset of the problem is very abrupt, so that the measurements of less than 120 m/s were satisfactory.

The problem can be resolved in a straightforward manner, but additional equipment is required. The object is to ensure that the measurable harmonic content is far in frequency from the Doppler signal, far enough that it can be effectively filtered out. There are several methods of accomplishing this. The velocity-to-frequency conversion factor can be reduced so that the Doppler frequency (down-shifted from the Bragg frequency) does not approach the high-pass cutoff frequency required to eliminate the harmonics. Another approach is to upshift the downstream velocity component from the Bragg frequency and then downshift it electronically to pass through the transmission line. Or, finally, the Bragg cell can be shut off when there is no directional ambiguity. The first method requires additional optics; the second needs added electronics and, probably, a sensor for the computer to know when it is operating. The last method requires no additional apparatus but necessitates realignment whenever the Bragg cell state is changed and hence becomes the most time consuming.

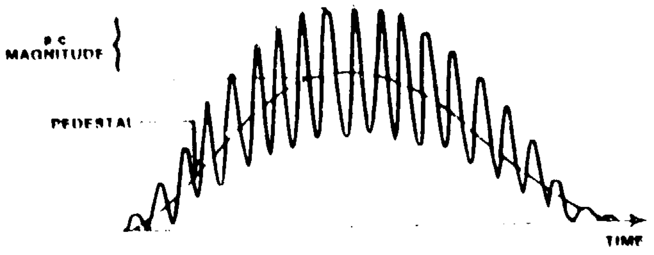

Figure C.1. Representative Drawing to Illustrate Doppler Burst and Pedestal Signal Received by an LDA Detector.

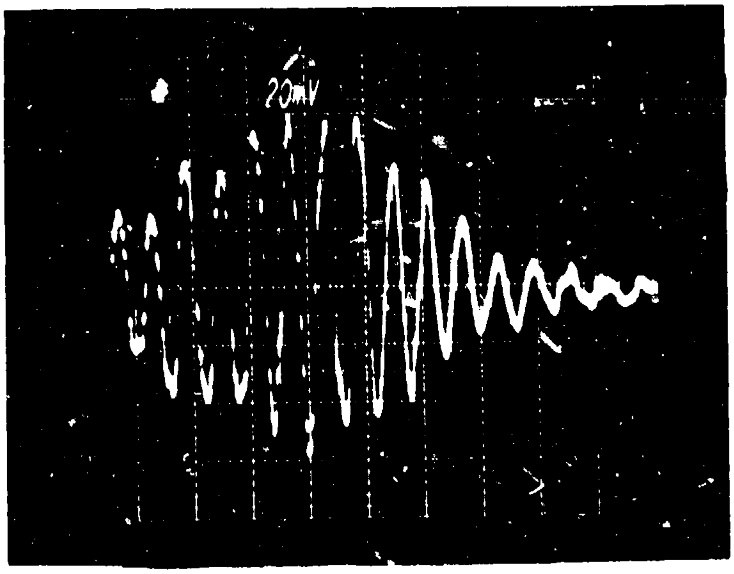

Figure C.2. Typical Doppler Burst Signal after Filtering has Eliminated the Pedestal Component.

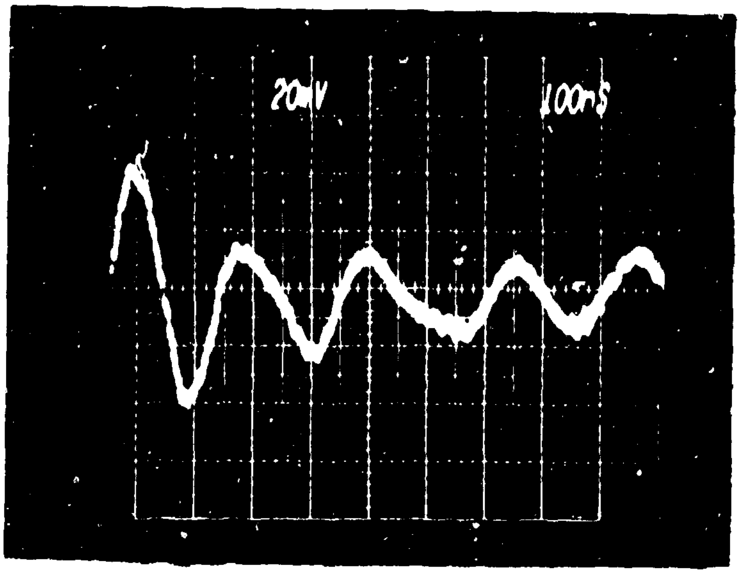

(a)

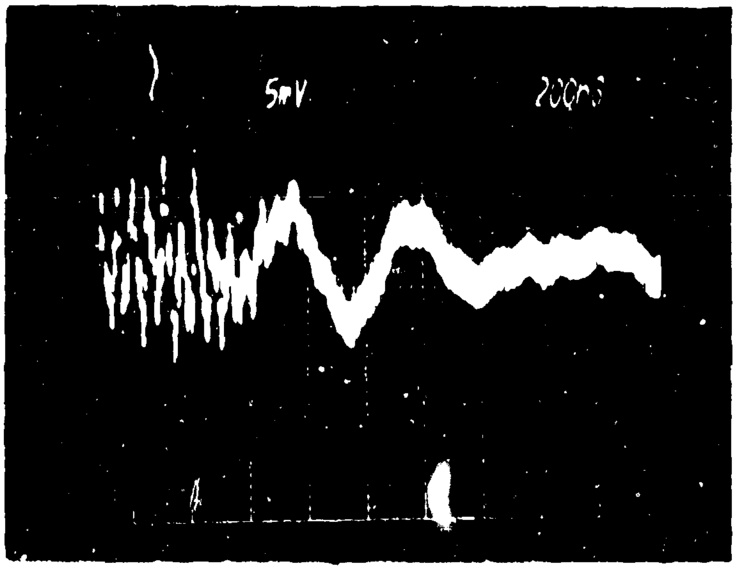

(b)

Figure C.3. Signals Passed by a High-Pass Filter Set at 5 MHz. (a) Pedestal harmonics alone; (b) Interference between Doppler burst and pedestal harmonics.

REFERENCES

1. A. J. Lightman and P. D. Magill, *Computer Software and Interfacing for the One-Dimensional Laser Doppler Anemometer*, University of Dayton Research Institute Technical Report UDR-TR-80-89, October 1980.

2. F. Durst, A. Melling, and J. H. Whitelaw, *Principles and Practices of Laser-Doppler Anemometry*, Academic Press, NY, 1976.

3. M. Glass and I. M. Kennedy, "An Improved Seeding Method in High Temperature Laser Doppler Velocimetry," Combustion and Flame, 29, pp. 333-335, 1977.

4. W. T. Mayo, Jr., M. T. Shay, and S. Ritter, *Proceedings of the Second International Workshop on Laser Velocimetry*, Purdue University, W. Lafayette, IN, 1974, pp. 16-26.

5. P. T. Harsha, *Free Turbulent Mixing: A Critical Evaluation of Theory and Experiment*, AEDC-TR-71-36, AEDC, TN, February 1971.

6. P. O. Witze, A. I. A. A. J. 12, pp. 417-418, 1974.

7. S. I. Pai, *Fluid Dynamics of Jets*, Van Nostrand Company, Inc., NY, 1954.

8. J. C. Lau, P. J. Morris, and M. J. Fisher, J. Fluid. Mech., 93, pp. 1-27, 1979.

9. A. A. Townsend, *The Structure of Turbulent Shear Flow*, Cambridge University Press, Cambridge, 1956.

10. D. F. G. Durao and J. H. Whitelaw, "Velocity Characteristics of Disc-Stabilized Diffusion and Premixed Flames," AIAA-76-34, January 1976.

11. D. F. G. Durao and J. H. Whitelaw, "Velocity Characteristics of the Flow in the Near Wake of a Disk," J. Fluid Mech., 85, Part 2, pp. 369-385, 1978.

12. L. Krishnamurthy, *Isothermal Flowfield Predictions of Confined Coflowing Turbulent Jets in an Axisymmetric Bluff-Body Near Wake*, University of Dayton Research Institute Technical Report UDR-TR-80-105, December 1980.

13. W. M. Roquemore et al., "Preliminary Evaluation of a Combustor for Use in Modeling and Diagnostics Development," ASME Publication 80-GT-93, March 1980.

14. G. J. Sturgess, private communication.

15. A. J. Yule and N. A. Chigier, "Combustion-Transition Interaction in a Jet Flame," AIAA-80-0077, January 1980.

B.1. D. K. McLaughlin and W. G. Tiederman, Phys. Fluid, 16, pp. 2082-2088, 1973.

B.2. H. Schlichting, *Boundary Layer Theory*, McGraw-Hill, NY, 1968.

U S GOVERNMENT PRINTING OFFICE 1981—757-002/15